# Hydrodynamic analysis of marine floating photovoltaics under the influence of seabed topography and coastlines*

Huajun Li[a], Qiujue Jiang[a], Deqing Zhang[a], Junfeng Du[a], Zhi-Ming Yuan[b], Anteng Chang[a,*]

[a]*College of Engineering, Ocean University of China, Qingdao, 266100, PR China*

[b]*Department of Naval Architecture, Ocean & Marine Engineering, University of Strathclyde, Glasgow, G4 0LZ, UK*

---

**Abstract**

Marine floating photovoltaics (MFPV) systems emerge as a promising frontier in the development of offshore clean energy, with their primary applications being in nearshore shallow waters. In these areas, the shallow depths, intricate seabed topographies and rugged shorelines profoundly affect wave propagation and transformation processes, leading to highly inhomogeneous wave conditions and thereby rendering traditional hydrodynamic theories based on assumptions of open seas inadequate. This study employs a hybrid Boussinesq-Panel Method (HBPM) to incorporate the effects of topography on wave dynamics into hydrodynamic calculations, striking a balance between computational accuracy and efficiency. A series of validation cases demonstrate the accuracy and necessity of the HBPM in shallow water environments. Computational results from typical bay scenarios reveal that variations in water depth and coastline reflections create multidirectional, non-uniform wave fields, which lead to complex force and motion characteristics of the structure. To ensure structural integrity, it is recommended to select installation sites located away from the breakwater entrance and close to the breakwater itself.

*Keywords*: Marine floating photovoltaics; Shallow water; Topography-impacted hydrodynamics; Boussinesq model; Panel method

---

## 1. Introduction

In 2022, non-clean energy sources constituted a substantial 80% of the global energy supply. The combustion of non-clean energy sources, such as coal, oil, and natural gas, produces various hazardous substances and significant carbon dioxide emissions that impact the ecosystem and contribute to the greenhouse effect. Solar energy, a clean energy source, is projected to grow rapidly over the next two decades and is expected to comprise 10% of the global energy supply by 2050 [1]. The primary method of harnessing solar energy is photovoltaic (PV) technology, which directly converts solar radiation into electrical energy via PV modules, most of which are silicon-based. Although conventional ground-mounted PV (GMPV) solar farms have been developed for a long time with mature technologies, land resources are scarce in

---

[*] Corresponding author.

*E-mail address:* changanteng@ouc.edu.cn (Anteng Chang).

This is a peer-reviewed, accepted author manuscript of the following article: Li, H., Jiang, Q., Zhang, D., Du, J., Yuan, Z.-M., & Chang, A. (2024). Hydrodynamic analysis of marine floating photovoltaics under the influence of seabed topography and coastlines. Ocean Engineering, 314(Pt. 2), Article 119708. https://doi.org/10.1016/j.oceaneng.2024.119708

high-energy consumption areas, such as populated cities, where high-rise buildings provide excessive shading, making large-scale GMPV solar farms unsuitable [2].

To advance clean energy development while ensuring the proper utilization of land resources, the concept of floating photovoltaics (FPV) has been introduced. FPVs are installed in inland lakes, reservoirs, and oceans, and typically consist of floating structures, connection systems, moorings and anchorages, inverters, underwater or overwater cables, and solar panels with their support structures [3]. Specifically, FPVs deployed in the ocean are referred to as marine floating photovoltaics (MFPV). Compared to GMPV, MFPV offers several advantages, including the conservation of land resources [4-8]; enhanced power generation efficiency due to the natural cooling effect of water bodies [9-12]; reduced impact from dust [5], [13,14] and shading [15,16]; and lower electricity transportation costs due to proximity to coastal energy-consuming areas [17].

Different forms of MFPV systems have been proposed by numerous researchers. Jiang et al. [3] designed a soft-connected MFPV system, and it is verified by experiments and numerical calculations that it can survive extreme harsh environmental conditions with wave heights exceeding 10 m. A lightweight with high stiffness floating platform is designed to support an MFPV by Jin et al. [18], the corresponding analytical solution to the hydrodynamic-structural-materials problem for this structure is presented by using the eigenfunction expansion method under the assumption of zero draft. Y. Shi et al. [19] used a frequency-domain approach to analyze the hydroelastic response of the floating photovoltaic structure under wave action. Li et al. [20] analyze the hydroelasticity of a modular floating structure (MFS) with multidirectional hinge connections designed for FPV systems by coupling the ABAQUS and WAMIT, and the analysis results show that the response of the structure becomes more pronounced as the structural stiffness increases. Song et al. [21] perform a braced frame response analysis of a multibody MFPV using AQWA and OrcaFlex, and investigate the effects of the axial stiffness of the tensioned mooring, and the arrangement angle of the MFPV system on the response of the braced frame under irregular waves. Claus et al. [22] proposed a design process for pontoon-type MFPV, in which both wind and wave loads are considered, and the motion response of rigid and hinged MFPV systems under different wind and wave conditions are systematically investigated. Zhang et al. [8] present the design, full-scale experiments, numerical validation model, and evaluation of the operational performance and power generation of the MFPV farm installed off the coast of Woodlands, Singapore. Choi et al. [23] use the computational fluid dynamics (CFD) method to calculate wind loads and the boundary element method (BEM) to calculate hydrodynamic coefficients, and validate the results through physical experiments. The results of the two calculations are used as boundary conditions for finite element method (FEM) analysis to assess the structural safety of the MFPV system under extreme environmental conditions. Bassam et al. [24] design a MFPV structure that is partially underwater, utilizing the underside of the tilted PV panels in direct contact with the water body to improve cooling performance.

However, current hydrodynamic analyses of MFPVs predominantly rely on linear potential theory, assuming these systems are deployed in unobstructed sea areas with horizontal seabed. This approach represents an adaptation and extension of conventional hydrodynamic analysis methods employed for marine engineering structures. MFPV systems are frequently designed as modular arrays consisting of lightweight individual modules [25,26], characterized by their shallow drafts, susceptibility to severe wind and wave conditions, and substantial requirements for operational and maintenance efforts. Currently, MFPV applications are primarily concentrated in nearshore shallow water areas (e.g., the two nearshore MFPV projects shown in Fig. 1). The shallow depths, intricate seabed contours, and twisting coastlines profoundly influence wave dynamics, resulting in changes in wave properties and significant shifts in the primary propagation direction due to phenomena such as refraction, reflection, and breaking. Consequently, the composition of wave fields in nearshore zones markedly differs from that in offshore environments. Traditional methods fall short in capturing the spatial and temporal evolution of waves, leading to inaccuracies in determining hydrodynamic coefficients during the initial design phase.

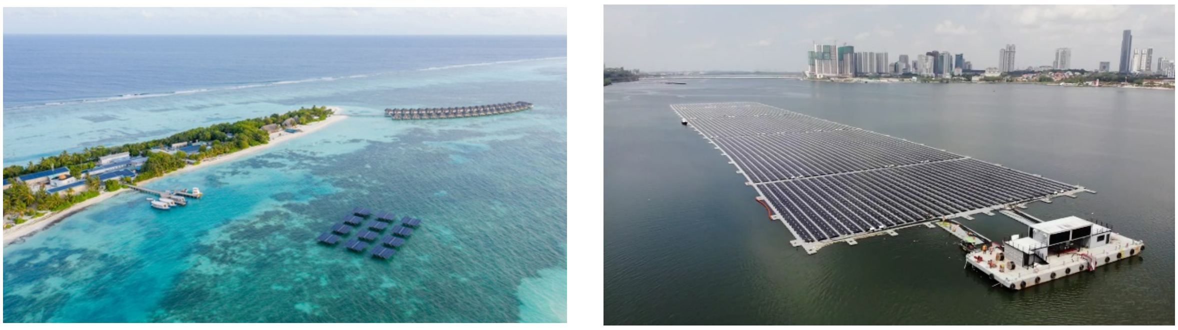
(a) (b)

Fig. 1. (a) SolarSea project by Swimsol near Maldives islands [27], (b) MFPV system by Sunseap near Woodlands Coast [28].

Modern hydrodynamic analysis models can incorporate topographic influences, making them suitable for evaluating hydrodynamics under varying water depths and coastline effects. These models include linear potential theory (second-body theory based on the free-surface Green function [29,30], Rankine source method [31,32]), fully nonlinear potential flow (FNPF) theory [33-35], and computational fluid dynamics methods (CFD) [36-39]. Despite their capabilities, these methodologies face challenges related to computational accuracy and efficiency. Concerning computational inaccuracies, linear potential theory can yield erroneous results if the dimensions and shapes of the second body are misrepresented. Moreover, while the linear Rankine source method can accommodate topographic variations through boundary condition adjustments, it fails to accurately capture significant nonlinear wave deformations and wave-wave interactions. Concerning computational efficiency, both FNPF and CFD methods experience a substantial decrease in efficiency as the simulation domain expands, complicating the modeling of extensive maritime areas spanning hundreds to thousands of meters. Additionally, for fully nonlinear time-domain simulation models, stability and numerical performance are critical factors that significantly constrain their applicability.

In port and coastal engineering, several shallow water wave models are commonly employed to efficiently capture the propagation dynamics of nearshore wave fields. These models include non-hydrostatic models, the Boussinesq equations, the mild-slope equation, and spectral wave models. Among these models, the Boussinesq equations are notable for their dimensional reduction and phase-resolving characteristics, which enable relatively rapid and accurate simulation of medium- and small-scale wave fields under complex topographic conditions. Over decades of development, various Boussinesq models with varying levels of accuracy have been established. Consequently, researchers have increasingly sought to integrate the Boussinesq equations with hydrodynamic analysis methods. Bingham [40] employed the Boussinesq equation, framed in terms of depth-averaged velocity, to compute wave excitation forces on a moored vessel within a harbor basin. Zheng et al. [41] coupled FUNWAVE-TVD with MIKE21-FRC and MIKE21-MA to explore the hydrodynamic impacts on a moored ship induced by seismic-induced oscillations in the harbor basin. Nevertheless, these efforts predominantly rely on free-surface Green functions as the fundamental solution for BEM calculations. These approaches are primarily applicable to open water or scenarios adjacent to vertical quays, rendering it ineffective for addressing the challenges posed by varying bottom terrain near floating structures. Some researchers have combined the Boussinesq equations with the BEM employing the Rankine source Green function. These studies primarily address the dynamic response of Very Large Floating Structures (VLFS) in near-island environments [42,43] . However, research on the hydrodynamic loads and motion responses of marine floating photovoltaics systems in variable-depth nearshore environments influenced by coastal reflections remains relatively limited.

To effectively integrate the impacts of topography and coastline into hydrodynamic analyses while optimizing computational accuracy and efficiency, this paper employs a hybrid numerical method, which combines the Boussinesq equation model with the Rankine-source-based panel model, to a novel MFPV structure. The inclusion of the Rankine source function, in contrast to the free-surface Green function, allows the hybrid Boussinesq-Panel Method (HBPM) to address the limitations associated with open water and flat seabeds, thereby facilitating more precise hydrodynamic calculations under complex topographic conditions.

The remainder of this paper is organized as follows: Chapter 2 details the MFPV structures under investigation and the implementation principles of the HBPM. Chapter 3 is dedicated to the validation of the numerical model. Chapter 4 examines the hydrodynamic characteristics of MFPV in a representative coastal region. Finally, Chapter 5 provides a summary and concludes the paper.

## 2. Detailed HBPM Description

This chapter begins by presenting a novel MFPV structure and the principles of the HBPM. The author's research team has independently designed a frame-based MFPV [25], as depicted in Fig. 2a. This design features a triangular steel frame supporting PV modules on the upper side, with 15 vertical high-density polyethylene (HDPE) pontoons on the lower side, which represent a typical material for MFPV pontoons [3]. The pontoons have a diameter of 2.2 m and a height of 1.6 m, with the centers of three pontoons forming an equilateral triangle with a side length of 10 m, ultimately creating a larger equilateral triangle with a side length of 40 m. Specific parameters are detailed in Table 1. Fig. 2b illustrates the proposed installation site, which is located in a shallow-water region surrounded by islands in the East China Sea. The shoaling effect of waves, wave-wave interactions, and coastline reflections render the linear potential theory, based on open water assumptions, inadequate. Furthermore, to mitigate wave impact and safeguard the MFPV, floating breakwaters will be installed at the bay entrance.

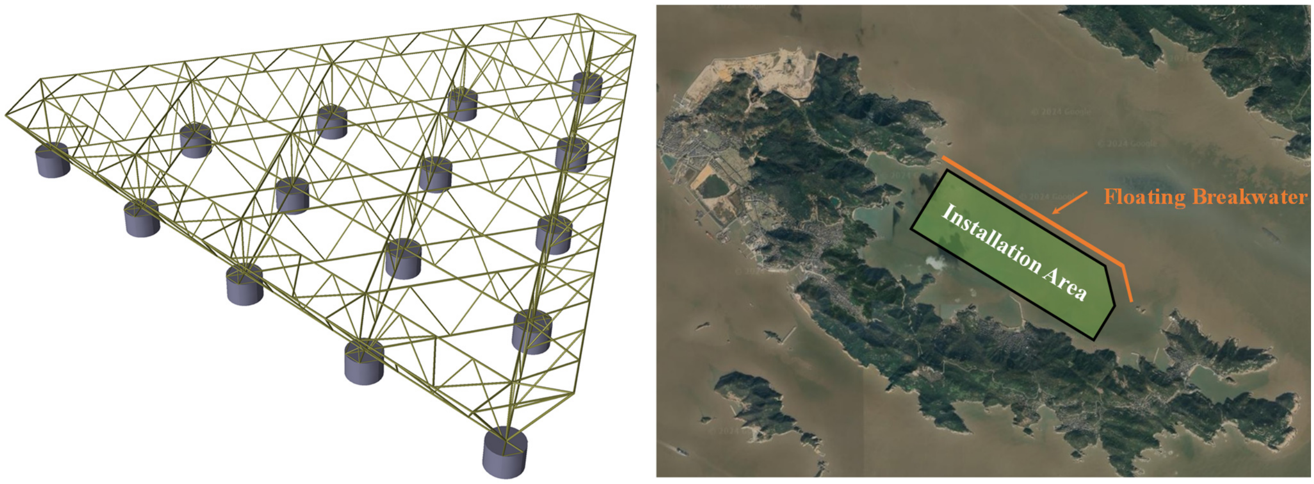

(a) (b)

Fig. 2. (a) Frame-Based MFPV model, (b) Projected installation site.

To address this issue, this paper proposes a hybrid Boussinesq-panel method, as illustrated in Fig. 3. *O-XYZ* is the global coordinate system, with the origin *O* fixed at the still water surface and the *Z*-axis oriented vertically upwards. The computational domain is strategically divided into two zones: the outer region, where wave field evolution is modeled using Boussinesq equations, and the inner region, where the hydrodynamic behaviors of the MFPV are analyzed through the panel model based on Rankine source method. Velocity and pressure field data, generated by the Boussinesq equations in the outer region, are conveyed to the inner region at the designated virtual interface, serving as boundary conditions for the inner domain after the time-to-frequency domain conversion. Therefore, the hybrid hydrodynamic analysis method established based on the above principles can account for the effects of complex shallow water environment on wave propagation and deformation. This enables efficient and accurate calculation of wave loads in typical shallow water topographies. Regarding the remainder of this chapter, Section 2.1 and Section 2.2 will discuss the fundamental theories of the numerical models involved in HBPM, while Section 2.3 will detail the specific implementation process of HBPM.

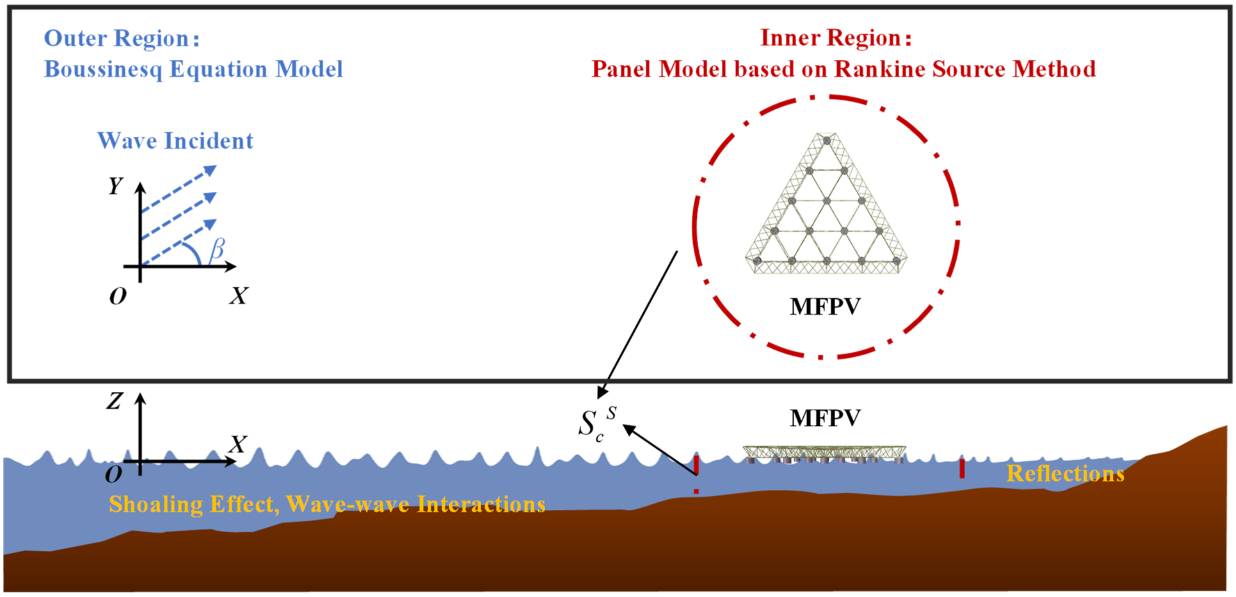

Fig. 3. Schematic diagram of HBPM.

Table 1 Detailed Parameters of MFPV

| Parameters | Unit | Value |
|---|---|---|
| Number of pontoons | | 15 |
| Length | m | 45.20 |
| Width | m | 44.50 |
| Total weight | t | 63.96 |
| Draft | m | 1.10 |
| Displacement *V* | $m^3$ | 62.40 |
| Radius of gyration *RX* | m | 10.83 |
| Radius of gyration *RY* | m | 10.83 |
| Radius of gyration *RZ* | m | 15.29 |

### *2.1. Panel Model: Inner Region*

Fig. 4 illustrates the triangular MFPV and the corresponding right-handed coordinate system. *o-xyz* is the body-fixed coordinate system of MFPV, and the origin *o* is located on the calm water surface and situated at the centroid of the triangle formed by the center points of the outer pontoons. The translational motions of the MFPV in the *x*, *y*, and *z* directions are defined as surge, sway, and heave, while the rotational motions around the three coordinate axes are defined as roll, pitch and yaw, respectively.

Assuming that the MFPV is positioned in an inviscid, incompressible fluid, the irrotational fluid motion can be described by a velocity potential that satisfies Laplace's equations. The velocity potential can be denoted by applying the principle of superposition as

$$\varPhi = \mathrm{Re}[\phi \mathrm{e}^{-\mathrm{i}\omega t}] = \mathrm{Re}\left[\left(\phi_S + \sum_{j=1}^{6}\xi_j\phi_j\right)\mathrm{e}^{-\mathrm{i}\omega t}\right] \tag{1}$$

where $\varPhi$ is the total potential; $\mathrm{Re}[\cdot]$ denotes the real part of the variable; $\phi_S$ is the complex scattering potential, consisting of the incident wave field and the perturbation by the fixed body; $\phi_j$ $(j = 1,2, \dots ,6)$ is the complex radiation potential induced by the unit velocity in the $j$-direction; $\xi_j$ is the complex amplitude of motion in the $j$-direction; $\omega$ is the angular frequency of incident wave.

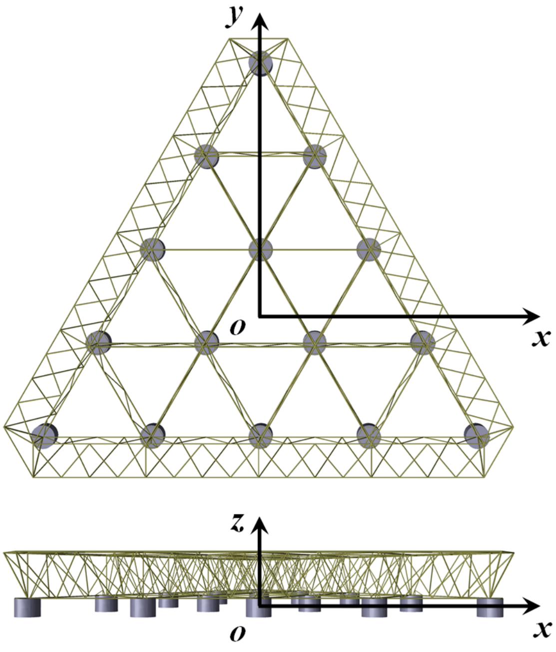

Fig. 4. Triangular MFPV and coordinate systems.

Note that, since radiation and scattering potentials can be solved independently and satisfy different control surface boundary conditions, two separate computational domains and corresponding meshes are established. However, the computational domain boundary types are all of the following four types: (a) mean wetted body surface $\left(S_b^R, S_b^S\right)$, (b) undistrubed free surface $\left(S_f^R, S_f^S\right)$, (c) control surface $\left(S_c^R, S_c^S\right)$, (d) seabed surface $\left(S_d^R, S_d^S\right)$. The governing equations and boundary conditions for the radiation and scattering potentials are as follows

(1) radiation potential

$$
\begin{aligned}
\nabla^2\phi_j &= 0, && j=1,2,\ldots,6 \ \text{ in fluid domain } \Omega^R \\
\frac{\partial\phi_j}{\partial n} &= -\mathrm{i}\omega n_j, && j=1,2,\ldots,6 \ \text{ on } S_b^R \\
\frac{\partial\phi_j}{\partial z}-\frac{\omega^2}{g}\phi_j &= 0, && j=1,2,\ldots,6 \ \text{ on } S_f^R \\
\sqrt{r}\left(\frac{\partial\phi_j}{\partial r}-\mathrm{i}k_0\phi_j\right) &= 0, && j=1,2,\ldots,6 \ \text{ on } S_c^R \\
\frac{\partial\phi_j}{\partial n} &= 0, && j=1,2,\ldots,6 \ \text{ on } S_d^R
\end{aligned}
\tag{2}
$$

where $g$ is the gravitational acceleration; $k_0$ is the local wave number derived from the water depth at the center of MFPV; $r = \sqrt{x^2 + y^2}$. $n_j$ is the generalized unit normal vector directed to the interior of the mean wetted body surface

$$
n_j = \begin{cases} \vec{n}, & j=1,2,3 \\ \vec{x}\times\vec{n}, & j=4,5,6 \end{cases}
\tag{3}
$$

where $\vec{x} = (x, y, z)$ is the position vector on the mean wetted surface $S_b^R$.

The radiation boundary condition in Eq. (2) (the fourth equation) is referred to as the Sommerfeld radiation condition. This condition is an artificially constraint intended for application at infinity, where it signifies that the radiation wave has a finite amplitude and propagates outward. The term $\sqrt{R}$ represents the amplitude of the radiation wave, decaying at a rate of $1/\sqrt{R}$, which ensures non-decaying terms are eliminated. This condition is often applied to the radiation control surface in Rankine source calculations, under the assumption that the control surface lies at a sufficiently distant location. Note that the optimal radius for the radiation control surface is determined by comparing Rankine source calculation results with those from commercial hydrodynamic software (WADAM) in this paper.

(2) scattering potential

$$
\begin{aligned}
\nabla^2\phi_S &= 0, && j=1,2,\ldots,6 \ \text{ in fluid domain } \Omega^S \\
\frac{\partial\phi_S}{\partial n} &= 0, && j=1,2,\ldots,6 \ \text{ on } S_b^S \\
\frac{\partial\phi_S}{\partial z}-\frac{\omega^2}{g}\phi_S &= 0, && j=1,2,\ldots,6 \ \text{ on } S_f^S \\
\frac{\partial\phi_S}{\partial n} &= 0, && j=1,2,\ldots,6 \ \text{ on } S_d^S
\end{aligned}
\tag{4}
$$

In addition to the above conditions, the boundary condition on the control surface $S_c^S$ is required to complete the scattering problem, the details of which will be presented in Section 2.3.

After the radiation and scattering potentials are solved, the pressure acting on the MFPV can be calculated based on the linearized version of Bernoulli equation

$$
p = \mathrm{i}\omega\rho\left(\phi_S + \sum_{j=1}^{6}\xi_j\phi_j\right)
\tag{5}
$$

where $\rho$ is the fluid density.

Hence, integrating the pressure over the mean wetted surface $S_b^S$ and $S_b^R$ yields the scattering and radiation wave forces

$$F_i^S = \mathrm{i}\omega\rho \iint_{S_b^S} \phi_S n_i \mathrm{d}S \qquad i = 1, 2, \ldots, 6 \tag{6a}$$

$$F_i^R = \mathrm{i}\omega\rho \sum_{j=1}^{6} \xi_j \iint_{S_b^R} \phi_j n_i \mathrm{d}S = \sum_{j=1}^{6} \left(\omega^2 \mu_{ij} + \mathrm{i}\omega\lambda_{ij}\right)\xi_j \qquad i = 1, 2, \ldots, 6 \tag{6b}$$

where $F_i^S$ is the scattering wave force in *i*-th direction; $\mu_{ij}$ and $\lambda_{ij}$ are the added mass coefficient and potential damping coefficient in the *i*-th direction induced by the *j*-th radiation motion

$$\mu_{ij} = \mathrm{Im}\left[ -\frac{\rho}{\omega} \iint_{S_b^R} \phi_j n_i \mathrm{d}S \right], \qquad i = 1, 2, \ldots, 6 \quad j = 1, 2, \ldots, 6 \tag{7a}$$

$$\lambda_{ij} = \mathrm{Re}\left[ \rho \iint_{S_b^R} \phi_{Rj} n_i \mathrm{d}S \right], \qquad i = 1, 2, \ldots, 6 \quad j = 1, 2, \ldots, 6 \tag{7b}$$

The linear equation of motion of the MFPV is obtained from Newton's second law

$$\sum_{j=1}^{6} \left[ -\omega^2 \left( M_{ij} + \mu_{ij} \right) - \mathrm{i}\omega\lambda_{ij} + K_{ij} \right] \xi_j = F_i^S, \qquad i = 1, 2, \ldots, 6 \tag{8}$$

where $M_{ij}$ is the generalized mass matrix of the MFPV and $K_{ij}$ is the restoring matrix.

The boundary element method developed by Hess and Smith [44] is employed for solving scattering and radiation problems. It is assumed that the source density $\sigma(\vec{q})$ is distributed over the surfaces ($S_b^S$, $S_f^S$, $S_c^S$ and $S_b^R$, $S_f^R$, $S_c^R$ ) of the computational domain, and $\vec{q} = (x_0, y_0, z_0)$ is the position vector of the source point on the boundary surface, then the potential in the fluid domain can be expressed using the distribution of source density on the boundary

$$\phi(\vec{P}) = \iint_{S_\Omega} \sigma(\vec{q}) G(\vec{P}, \vec{q}) \mathrm{d}S_{\vec{q}} \tag{9}$$

where $\vec{P} = (x, y, z)$ is an arbitrary point in the fluid domain, $G\left(\vec{P}, \vec{q}\right)$ is the Rankine type Green function which satisfied the impenetrable seabed boundary condition

$$G(\vec{P}, \vec{q}) = \frac{1}{\sqrt{(x - x_0)^2 + (y - y_0)^2 + (z - z_0)^2}} + \frac{1}{\sqrt{(x - x_0)^2 + (y - y_0)^2 + (z + z_0 + 2h_0)}} \tag{10}$$

where $h_0$ is the water depth.

Taking normal derivatives on both sides of Eq. (9) and discretizing the computational domain surface $S_\Omega$ into $N$ elements with constant source density, and then making $\vec{P}$ converge to the centroid of each element (still denoted by $\vec{P}$), obtaining a set of linear equations, as shown in Eq. (11a). Eq. (9) can similarly be expressed in discrete form using the same approach, as presented in Eq. (11b).

$$\frac{\partial\phi\left(\vec{P}_m\right)}{\partial n_{\vec{P}_m}}=2\pi\sigma\left(\vec{P}_m\right)+\sum_{\substack{n=1\\ m\neq n}}^{N}\sigma\left(\vec{q}_n\right)\iint_{S_\Omega}\frac{\partial G\left(\vec{P}_m,\vec{q}_n\right)}{\partial n_{\vec{P}_m}}\mathrm{d}S_{\vec{q}_n},\quad m=1,2,\ldots,N,\quad n=1,2,\ldots,N \tag{11a}$$

$$\phi\left(\vec{P}_m\right)=\sum_{n=1}^{N}\sigma\left(\vec{q}_n\right)\iint_{S_\Omega}G\left(\vec{P}_m,\vec{q}_n\right)\mathrm{d}S_{\vec{q}_n},\quad m=1,2,\ldots,N,\quad n=1,2,\ldots,N \tag{11b}$$

The source strength can be solved separately by substituting corresponding boundary conditions into Eq. (11). After substituting the corresponding boundary conditions for the radiation and scattering potentials into Eq. (11), rearranging and combining them results in a system of linear equations with $N$ unknowns. These unknowns represent the Rankine source strengths on each element, and solving the system yields the source strengths for each element. For the radiation potential, the number of equations matches the number of unknowns, allowing for a direct solution. However, for the scattering potential, the number of equations exceeds the number of unknowns, making a direct solution impossible. This discrepancy arises due to the boundary conditions at the control surface, and the process for solving the scattering potential will be detailed in Section 2.3. After determining the source strengths of the radiation potentials, the added mass and potential damping are performed in accordance with Eq. (7).Note that the analytic expression for the second term on the right-hand side of Eq. (11) can be found in [44].

### *2.2. Boussinesq Equation: Outer Region*

Over more than a decade of development, the open-source, fully nonlinear Boussinesq model FUNWAVE-TVD [45] has evolved into a powerful tool for simulating the propagation and evolution of coastal wave fields [44-46]. Numerous researchers have validated its computational accuracy for simulating nearshore wave phenomena, including refraction, diffraction, breaking, and nonlinear wave interactions. The horizontal velocity distribution used in FUNWAVE-TVD has the same form as in NWOGU's work [49]

$$\mathbf{u}=\mathbf{u}_\alpha+\mathbf{u}_2(z) \tag{12}$$

$\mathbf{u}_\alpha=\left(u_\alpha,v_\alpha\right)$ is the horizontal velocity vector at the reference elevation $z=z_\alpha$. In contrast to NWOGU's work, Kennedy [50] defines $z_\alpha$ as a time-dependent variable

$$z_\alpha=\zeta h+\beta\eta \tag{13}$$

where $h$ is local still water depth, $\eta$ is local surface elevation and $\zeta$ and $\beta$ are constants. In the NWOGU's article [49], the value of $z_\alpha$ is rationally chosen with the aim of optimizing the dispersion relation of the Boussinesq model. Thus the default values of $\zeta$ and $\beta$ are -0.53 and 0.47.

$$\mathbf{u}_2(z)=\left(z_\alpha-z\right)\nabla A+\frac{1}{2}\left(z_\alpha^2-z^2\right)\nabla B \tag{14}$$

represents the depth-dependent correction, where $A$ and $B$ are denoted as

$$\begin{aligned} A &= \nabla \cdot (h\mathbf{u}_\alpha) \\ B &= \nabla \cdot \mathbf{u}_\alpha \end{aligned} \tag{15}$$

The governing equations for FUNWAVE-TVD are based on the work of Chen [51]. The dispersive effects are accurate to $O(\mu^2)$ and the nonlinear effects are accurate to all orders of $\epsilon$ (where $\mu = h/L; \epsilon = a/h; L$ and $a$ denote the wave length and amplitude).

The depth-averaged continuity equation is

$$\eta_t + \nabla \cdot \mathbf{M} = 0 \tag{16}$$

the horizontal volume flux $\mathbf{M}$ can be written as follows

$$\mathbf{M} = H(\mathbf{u}_\alpha + \bar{\mathbf{u}}_2) \tag{17}$$

where $H = h + \eta$ is the total local water depth and $\bar{\mathbf{u}}_2$ is the depth averaged horizontal velocity

$$\bar{\mathbf{u}}_2 = \frac{1}{H}\int_{-h}^{\eta} \mathbf{u}_2(z)\mathrm{d}z = \left(\frac{z_\alpha^2}{2} - \frac{1}{6}\left(h^2 - h\eta + \eta^2\right)\right)\nabla B + \left(z_\alpha + \frac{1}{2}(h-\eta)\right)\nabla A \tag{18}$$

The depth-averaged horizontal momentum equation can be written as

$$\mathbf{u}_{\alpha,t} + (\mathbf{u}_\alpha \cdot \nabla)\mathbf{u}_\alpha + g\nabla\eta + \mathbf{V}_1 + \mathbf{V}_2 + \mathbf{V}_3 + \mathbf{R} = 0 \tag{19}$$

where $\mathbf{R}$ represents diffusive and dissipative terms including bottom friction and subgrid lateral turbulent mixing. $\mathbf{V}_1$ and $\mathbf{V}_2$ are terms representing the dispersive Boussinesq terms given by

$$\mathbf{V}_1 = \left(\frac{z_\alpha^2}{2}\nabla B + z_\alpha \nabla A\right)_t - \nabla\left(\frac{\eta^2}{2}B_t + \eta A_t\right) \tag{20a}$$

$$\mathbf{V}_2 = \nabla\left[(z_\alpha - \eta)(\mathbf{u}_\alpha \cdot \nabla)A + \frac{1}{2} + (z_\alpha^2 - \eta^2)(\mathbf{u}_\alpha \cdot \nabla)B + \frac{1}{2} + (A + \eta B)^2\right] \tag{20b}$$

The term $\mathbf{V}_3$ in Eq. (19) represents the $O(\mu^2)$ contribution to the expression for $\boldsymbol{\omega} \times \mathbf{u} = \omega\mathbf{i}^z \times \mathbf{u}$ (with $\mathbf{i}^z$ the unit vector in the $z$ direction) and can be written as

$$\mathbf{V}_3 = \omega_0 \mathbf{i}^z \times \bar{\mathbf{u}}_2 + \omega_2 \mathbf{i}^z \times \mathbf{u}_\alpha \tag{21}$$

where

$$\omega_0 = (\nabla \times \mathbf{u}_\alpha) \cdot \mathbf{i}^z = v_{\alpha,x} - u_{\alpha,y} \tag{22a}$$

$$\omega_2 = (\nabla \times \mathbf{u}_2) \cdot \mathbf{i}^z = z_{\alpha,x}(A_y + z_\alpha B_y) - z_{\alpha,y}(A_x + z_\alpha B_x) \tag{22b}$$

### *2.3. Specific Implementation Process of HBPM*

The computational flowchart of the HBPM is shown in Fig. 5. The simulation of the HBPM consists of three major parts: (A) wave field calculations in the outer region, (B) transmission of the wave field information on $S_c^S$ and (C) BEM calculations in the inner region. The total velocity potential is decomposed into scattering and radiation potential respectively, so two corresponding sets of computational meshes are generated based on the secondary development of the commercial software HyperMesh. The outer region wave field is solved using FUNWAVE-TVD, where the topography and wave conditions are the fundamental information. Meanwhile, the virtual preset position of the computational mesh on $S_c^S$ in the outer region will be required, in order to configure the digital wave gauges to record the horizontal velocities $\mathbf{u}_\alpha(t)$ and the wave surface elevations $\eta(t)$ in FUNWAVE-TVD.

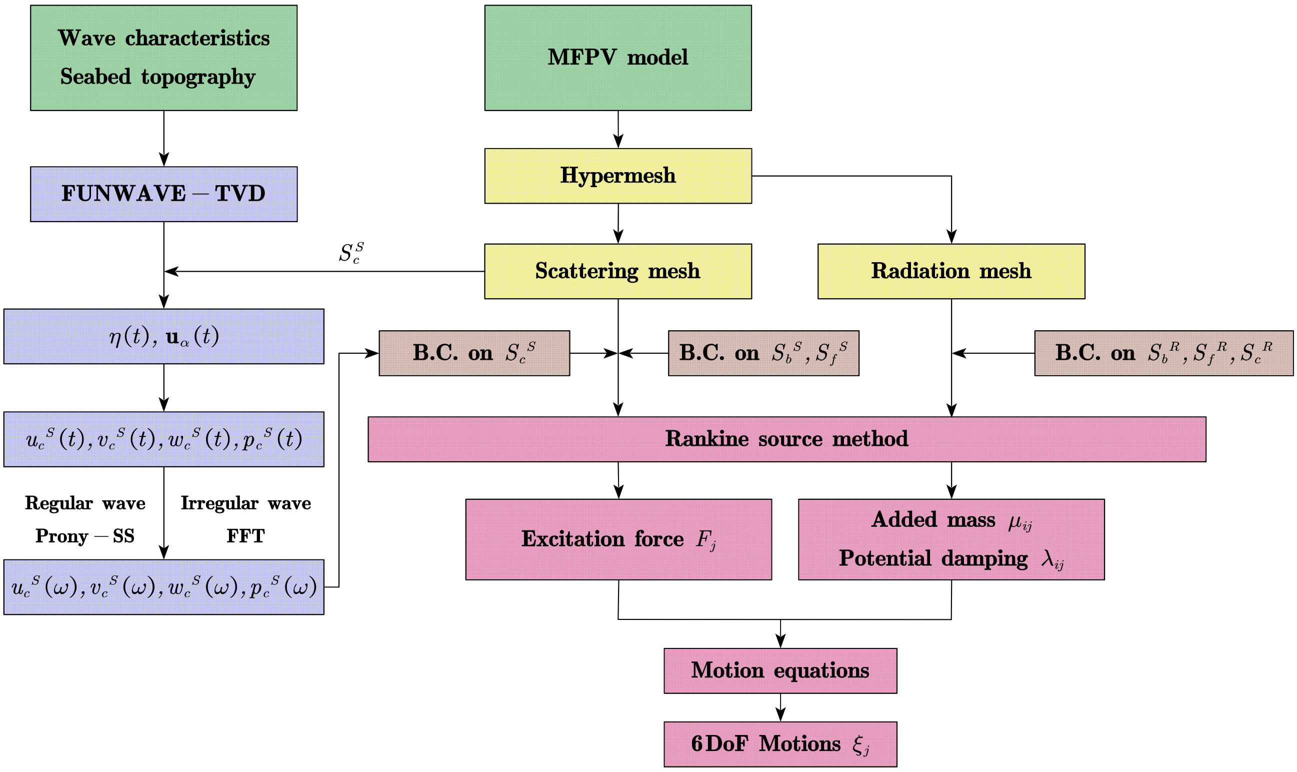

Fig. 5. Computational flowchart of HBPM.

Since the Boussinesq model has reduced dimensional characteristics, the vertical distribution of the vertical velocity $w$ is obtained by using Eq. (23)

$$w = -\nabla \cdot \left[ (z+h) \mathbf{u}_\alpha \right] \tag{23}$$

Furthermore, the pressure field [51] can be expressed as

$$\frac{p}{\rho} = g\eta + (z-\eta)\left\{ A_t + \frac{1}{2}(z+\eta)B_t + (\mathbf{u}_\alpha \cdot \nabla A) + \frac{1}{2}(z+\eta)(\mathbf{u}_\alpha \cdot \nabla B) - AB - \frac{1}{2}(z+\eta)B^2 \right\} \tag{24}$$

The vertical distribution of horizontal velocity is calculated by Eq. (12), (14) and (15). The first and second order derivatives involved in the calculations are computed using the difference method, taking the derivatives of the velocity field in the $x$ direction as an example

$$\begin{aligned}
\left(\frac{\partial u_\alpha}{\partial x}\right)_{i,j} &= \frac{u_\alpha^{(i+1,j)} - u_\alpha^{(i-1,j)}}{2\Delta x} \\
\left(\frac{\partial u_\alpha}{\partial y}\right)_{i,j} &= \frac{u_\alpha^{(i,j+1)} - u_\alpha^{(i,j-1)}}{2\Delta y} \\
\left(\frac{\partial^2 u_\alpha}{\partial x^2}\right)_{i,j} &= \frac{u_\alpha^{(i+1,j)} - 2u_\alpha^{(i,j)} + u_\alpha^{(i-1,j)}}{(\Delta x)^2} \\
\left(\frac{\partial^2 u_\alpha}{\partial y^2}\right)_{i,j} &= \frac{u_\alpha^{(i,j+1)} - 2u_\alpha^{(i,j)} + u_\alpha^{(i,j-1)}}{(\Delta y)^2} \\
\left(\frac{\partial^2 u_\alpha}{\partial x \partial y}\right)_{i,j} &= \frac{u_\alpha^{(i+1,j+1)} + u_\alpha^{(i-1,j-1)} - u_\alpha^{(i-1,j+1)} - u_\alpha^{(i+1,j-1)}}{4\Delta x \Delta y}
\end{aligned} \tag{25}$$

where $\Delta x, \Delta y$ is consistent with the spatial resolution in FUNWAVE-TVD, i.e., at least 60 grid points per wavelength range [52].

The $\mathbf{u}_\alpha(t)$ at the difference points is obtained using interpolation after the outer region calculation completed. The velocities time series $u_c^S(t), v_c^S(t), w_c^S(t)$, and dynamic pressure time series $p_c^S(t)$ at each element on $S_c^S$ are obtained using Eqs. (12)-(15), Eq. (23), (24) and (25). For the execution of calculations within the inner region, the aforementioned temporal series on the $S_c^S$ must be transformed into frequency domain components $u_c^S(\omega), v_c^S(\omega), w_c^S(\omega), p_c^S(\omega)$. With respect to time-frequency transformations, for regular waves we use the Prony-SS decomposition [53] and for irregular waves we use the Fast Fourier Transform (FFT). The Prony-SS decomposition assumes the signal as a linear combination of real or complex exponentials (Prony series), solving first-order difference equations based on state-space models. It can achieve high frequency resolution with relatively few sample points (we can attain a frequency resolution of $10^{-15}$ Hz in HBPM implementation using only 200 data points). In contrast, FFT is constrained by frequency resolution and struggles to distinguish closely spaced frequency components, often encountering leakage issues. Therefore, Prony-SS decomposition offers advantages in handling regular wave problems. However, as the number of frequency components increases, solving for higher-order Prony series coefficients becomes time-consuming.

To ensure the uniqueness of the scattering potential in the inner region, two sets of boundary conditions are used on at the $S_c^S$

$$\begin{aligned}
&\frac{\partial \phi_S}{\partial n} = \left[u_c^S(\omega), v_c^S(\omega), w_c^S(\omega)\right] \cdot \left(n_x, n_y, n_z\right) \\
&p_S = \mathrm{i}\omega\rho\phi_S = p_c^S(\omega)
\end{aligned} \tag{26}$$

Afterwards, the boundary conditions on $S_b^S, S_f^S$ and $S_c^S$ are substituted into Eq. (11) and amalgamated to form a system of linear equations for the scattering problem. Note that since there are two sets of boundary conditions on $S_c^S$, the coefficient matrix $[G]$ of the system of linear equations is not square, i.e., the number of equations, $M$, exceeds the number of unknowns, $N$. The generalized inverse method is employed to determine the least squares solution for this system of equations

$$[G]^T_{(N\times M)}[G]_{(M\times N)}[\sigma]_{(N\times 1)}=[G]^T_{(N\times M)}[b]_{(M\times 1)} \tag{27}$$

where $[\sigma]_{(N\times 1)}$ consists of the scattering source strength at each element, and $[b]_{(M\times 1)}$ is the constant term associated with the boundary conditions. After solving Eq. (27), the wave excitation forces can be computed from Eq. (6a) and (11b), and the motion of the MFPV can then be evaluated using Eqs. (6) - (8).

## 3. Method Verification

This section carries out the validation of the HBPM, which is divided into two parts: the scattering potential and radiation potential. Given that the panel model for the inner region is based on linear potential theory and the MFPV is anticipated to be situated in a nearshore environment shielded by the floating breakwater, the waves are considered to satisfy linear prerequisite

$$kA/\tanh\left(kh\right)\ll 1 \tag{28}$$

where $k$ is the wave number and $A$ is the amplitude. Throughout this paper, unless otherwise specified, this ratio is preset to $kA/\tanh(kh) = 0.05$.

### *3.1. Scattering potential*

In this section, we validate the scattering potential for the HBPM. Fig. 6 shows side views of three distinct terrain configurations, where $L_0$ and $L_{\mathrm{peak}}$ represent the wavelengths of regular waves and the peak frequency wavelengths of irregular waves, in accordance with the linear dispersion relation. Using these configurations, five validation examples (V1 - V5) are established, with specific parameters detailed in Table 2. Here, $h_{\mathrm{wm}}$ denotes the water depth at the wavemaker in FUNWAVE-TVD, and $h_{\mathrm{MFPV}}$ denotes the water depth at the MFPV. $T$ is the wave period for regular waves, $T_p$ is the peak period for irregular waves, $H$ is the wave height for regular waves, and $H_{\mathrm{sig}}$ is the significant wave height for irregular waves. The validation of the scattering potential fundamentally entails verifying the wave excitation forces, which is directly obtained by integrating the scattering potential over the mean wetted body surface. In traditional deep-sea engineering, common hydrodynamic calculations are based on the assumptions of open water and a flat seabed. In such settings, wave excitation forces are derived by combining the amplitude spectrum with the response amplitude operator (RAO) of wave forces. This RAO is calculated using linear potential theory, facilitated by the commercial software SESAM-WADAM, referenced in this study. Since WADAM also uses the panel method for hydrodynamic calculations, this method is referred to as the linear panel method (LPM).

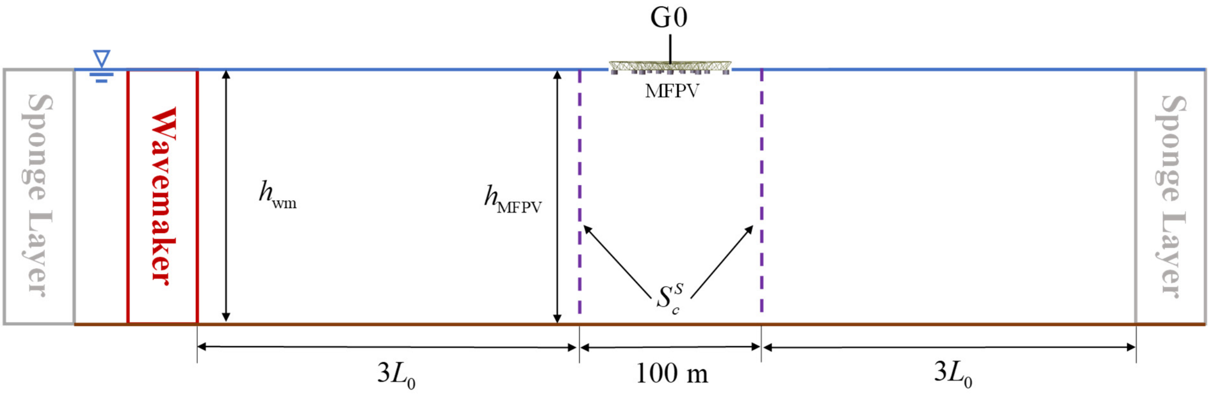

(a)

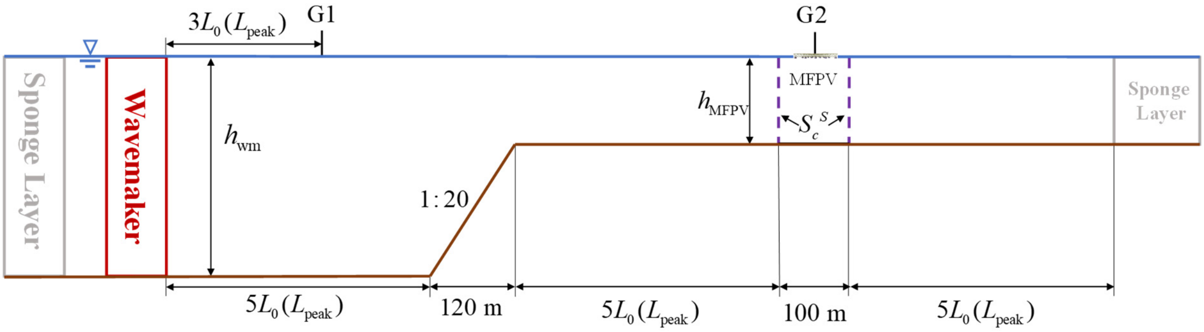

(b)

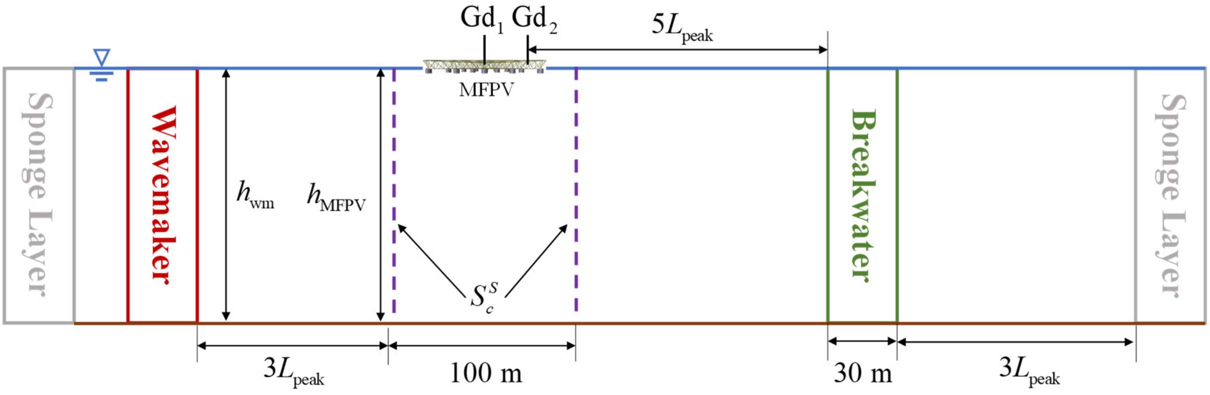

(c)

Fig. 6. Verification example side view schematic: (a) V1, (b) V2 - V4, (c) V5.

Table 2 Parameter of Verification Example

| No. | Topography | Wave Climate | Incident Angle/deg | $h_{\mathrm{wm}}$/m | $h_{\mathrm{MFPV}}$/m | $T(T_{\mathrm{p}})$/s | $H(H_{\mathrm{sig}})$/m |
|---|---|---|---|---|---|---|---|
| V1 | Flat | regular | 0 | 10 | 10 | 8 | 0.8 |
| V2 | Slope | regular | 0 | 10 | 4 | 8 | 0.8 |
| V3 | Slope | regular | 30 | 10 | 4 | 8 | 0.8 |
| V4 | Slope | irregular | 0 | 10 | 4 | 8 | 2.0 |
| V5 | Flat (breakwater) | irregular | 0 | 10 | 10 | 8 | 2.0 |

### *3.1.1. Flat Topography*

The objective of V1 is to validate the accuracy of the HBPM within the scope of linear potential theory. The inner region is located $3L_0$ from the wavemaker, with $S_c^S$ having a radius of 50 m. Sponge layers are positioned on the left and right sides of the computational domain to prevent wave reflection at the boundaries. The digital gauge G0 is used to record the time series of the wave surface elevation at the center of the MFPV and then transform it into frequency domain components using Prony-SS decomposition. The decomposition results are linearly superimposed with the wave excitation forces obtained from WADAM, resulting in the LPM output $F_0$. The FUNWAVE-TVD simulation for V1 encompasses a 200-second duration with a sampling frequency of 10 Hz. The final 50-second segment is reserved for conducting time-frequency analysis, with the preceding interval focused on establishing a stable wave field. Based on the revisited Le Méhauté diagram [54], the regular wave at point G0 is identified as falling within the second-order Stokes wave regime. Fig. 7 provides a detailed comparison between the numerical wave generation results and the theoretical solution for second-order Stokes waves, thereby validating the accuracy of wave generation through FUNWAVE-TVD.

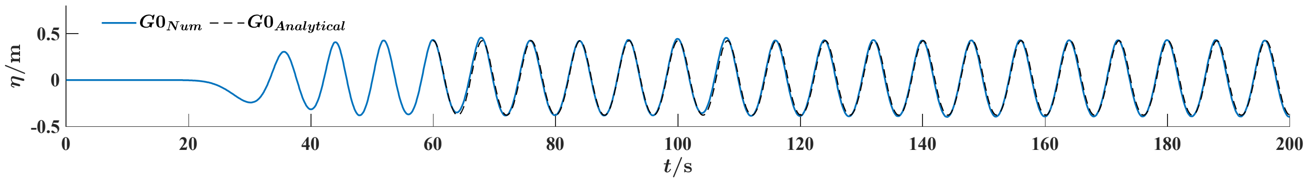

Fig. 7. Time series of wave surface elevation at G0.

The computational mesh for the inner region (Fig. 8) is crafted utilizing HyperMesh through the TCL secondary development script, allocating element counts of 5160, 6348, and 5109 for $S_b^S$, $S_f^S$, and $S_c^S$, respectively. To conserve computational time, a partition strategy is employed for free surface mesh, whereby domain distant from the body surface are allocated a lower mesh density. Fig. 9 presents the comparison between six-degree-of-freedom (6-DoF) wave excitation forces derived from the HBPM ($F_{\mathrm{hybrid}}$) and $F_0$, demonstrating notable alignment in all directions except for sway. In the sway direction, wave excitation forces exhibit certain differences in the higher harmonic components, which may be related to the resonance of transverse short waves between the pontoons. Importantly, sway excitation forces are considerably minor compared to those in the other five directions, thereby exerting minimal impact on subsequent analyses. Therefore, the comparisons in this section demonstrate the feasibility of HBPM and the reliability of its computational results. Note that the time-frequency conversion (either Prony-SS or FFT) results in frequency components at zero frequency. In the computation of the HBPM, these components are regarded as extremely low frequencies ($10^{-5}$ Hz), denoted as the 0th component.

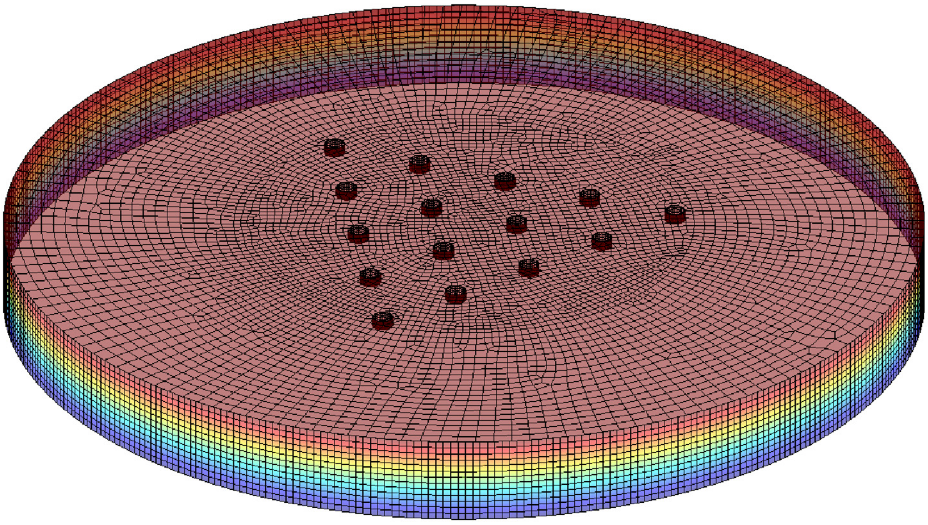

Fig. 8. The inner region computational mesh of V1.

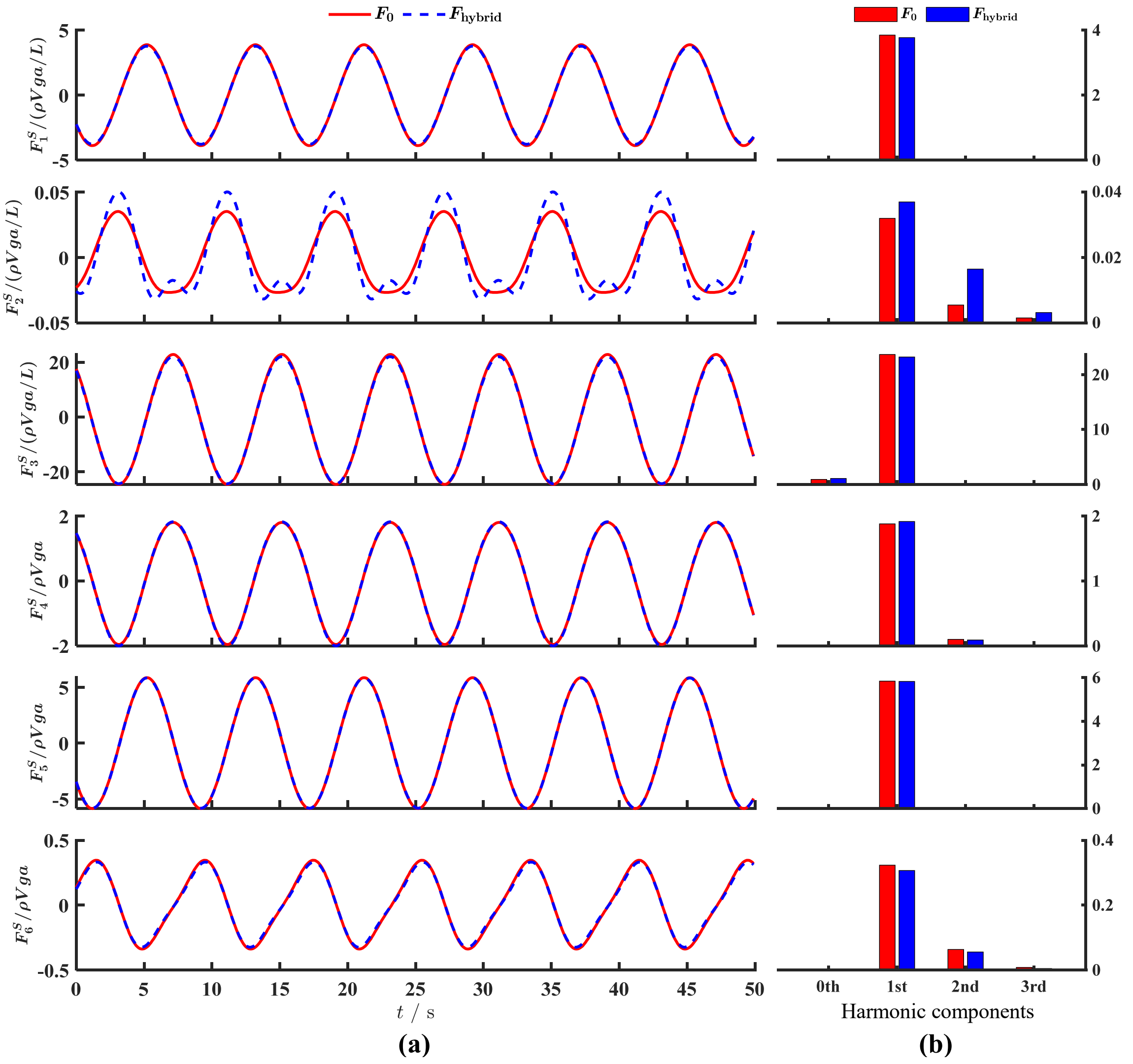

Fig. 9. 6-DOF wave forces comparison of V1: (a) time domain, (b) frequency domain.

### *3.1.2. Simplified Slope Topography*

A simplified model of a typical nearshore non-horizontal seabed consists of connecting two horizontal areas with an intervening slope. This approach treats both the open sea, with its reduced impact on wave propagation, and gently sloping banks as horizontal areas with varying water depths. As waves traverse sloping terrain, they experience the shoaling effect and become more nonlinear, resulting in distinct differences between waves beyond the slope and those in the open sea. Using wave data from the open sea for hydrodynamic computations in this context can result in significant inaccuracies. To assess the computational effectiveness of the HBPM under these conditions, we established an example with a slope of 1:20, where the water depths on the two sides are 10 m and 4 m (Fig. 6b). The wavemaker of FUNWAVE-TVD is located in the deep-water region, and the MFPV is placed in the shallower area. The distance between the slope and the wavemaker is $5L_0$ (for irregular waves, it is $5L_{\text{peak}}$). The inner region is positioned at a water depth of 4 m, and the distance from the end of the slope is $5L_0$. A sponge layer is positioned at the right boundary, $3L_0$

beyond the inner region, to simulate a coastline with coastal protection and wave-dissipating structures. The computational mesh remains consistent with that of V1 except for a water depth of 4 m, which reduces the number of elements on $S_c^S$ to 1965, consequently decreasing the computational load for the Prony-SS decomposition.

The FUNWAVE-TVD simulation for V2 is conducted over 300 s, with the final 50 s allocated for Prony-SS decomposition. A snapshot at $t$ = 250 s, shown in Fig. 10a, reveals significant transformations in the waves after traversing the slope: there is a noticeable increase in wave height, with crests becoming sharper and troughs flattening. These changes indicate a greater proportion of higher-order harmonic components. The comparison of wave elevation time series at G1 and G2 (Fig. 10b) further demonstrates that both the crests and troughs of waves beyond the slope are higher than those of the incident waves. Fig. 10c presents a comparison between the numerical wave generation results and the corresponding analytical solutions at G1 and G2. Owing to the increased nonlinearity of waves at G2 after traversing the slope (the wave at G2 falls within the third-order Stokes wave range in the revisited Le Méhauté diagram), Fenton's stream function theory [55] is adopted as the analytical solution for G2. After the wave field stabilized, the numerical results at both wave gauges aligned closely with the analytical solutions, showcasing the remarkable ability of FUNWAVE-TVD to capture wave nonlinear deformation.

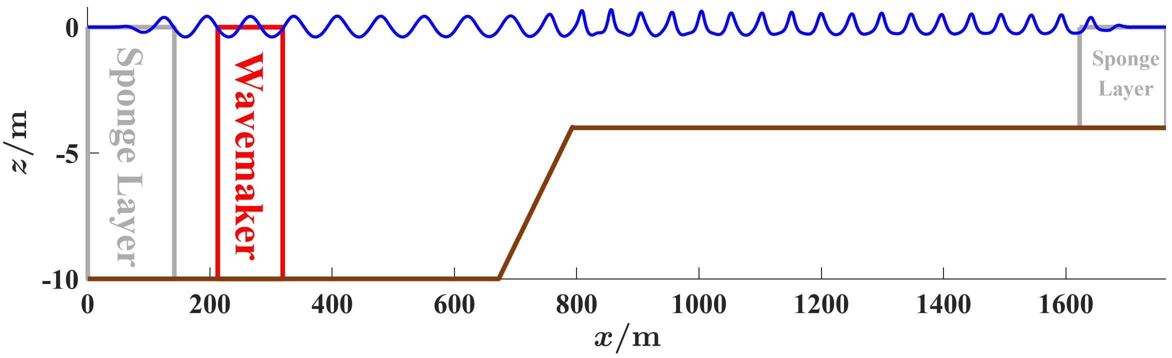

(a)

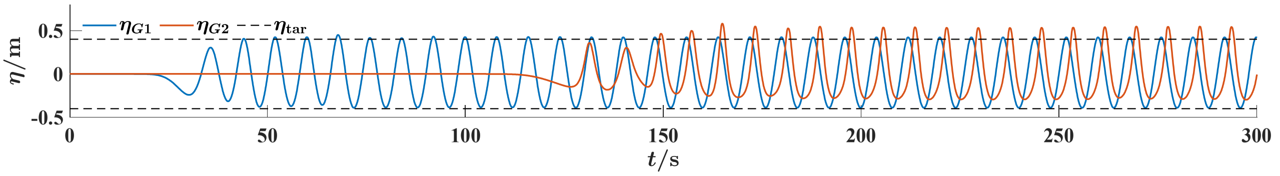

(b)

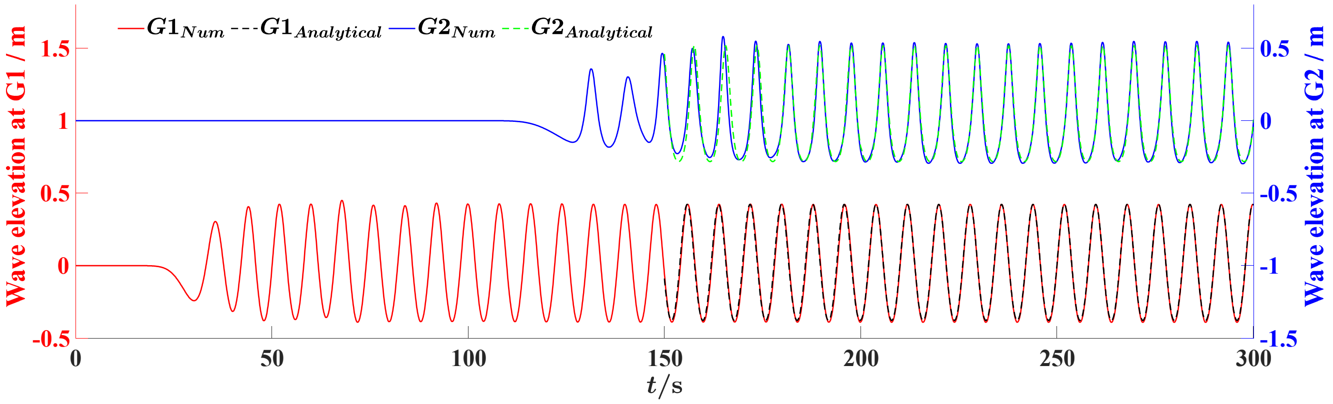

**(c)**

Fig. 10. (a) Snapshot of V2 wave field at $t = 250$ s, (b) Comparison of wave surface elevation of G1 and G2 in V2, (c) Comparison between the numerical wave generation results and corresponding analytical solutions (G1: second-order Stokes solution; G2: stream function solution).

In the context of slope examples involving two horizontal seabeds, there are two LPMs for calculating wave excitation forces: (i) multiplying the wave amplitude components at point G1 by the WADAM-determined forces for a water depth of 10 m, and (ii) multiplying the wave amplitude components at point G2 by the WADAM-determined forces for a water depth of 4 m. The RAOs for wave excitation forces, as computed by WADAM for water depths of 10 meters and 4 meters, are shown in Fig. 11.

Embedded within the LPM (i) and (ii) are two key assumptions: first, the floating structure is assumed to be situated in an unobstructed, flat sea during the calculation of wave excitation forces; second, the wave field's non-uniformity is assumed to be minimal, suggesting that spatial fixed-point data can serve as a reasonable approximation of the wave field surrounding the installation site. The primary distinction between these two methods lies in their respective uses of fixed-point wave data: the former utilizes data from the open sea, while the latter employs data from the structure's center. The implementation of a right-hand sponge layer to emulate a non-reflecting shoreline results in a comparably uniform wave field, keeping V2 within the operational scope of LPM (ii). Fig. 12 shows the forces obtained from the HBPM and the two LPMs. Similar to V1, a negligible numerical error occurs in the sway direction, contributing to the discrepancy between the hybrid yaw wave excitation force and that of LPM (ii). In the remaining four directions, the HBPM results closely align with those of LPM (ii). This comparison suggests that employing LPM (i) leads to inaccuracies in determining fundamental frequency wave excitation forces; notably, the wave excitation force in the heave direction is overestimated by almost 50%.

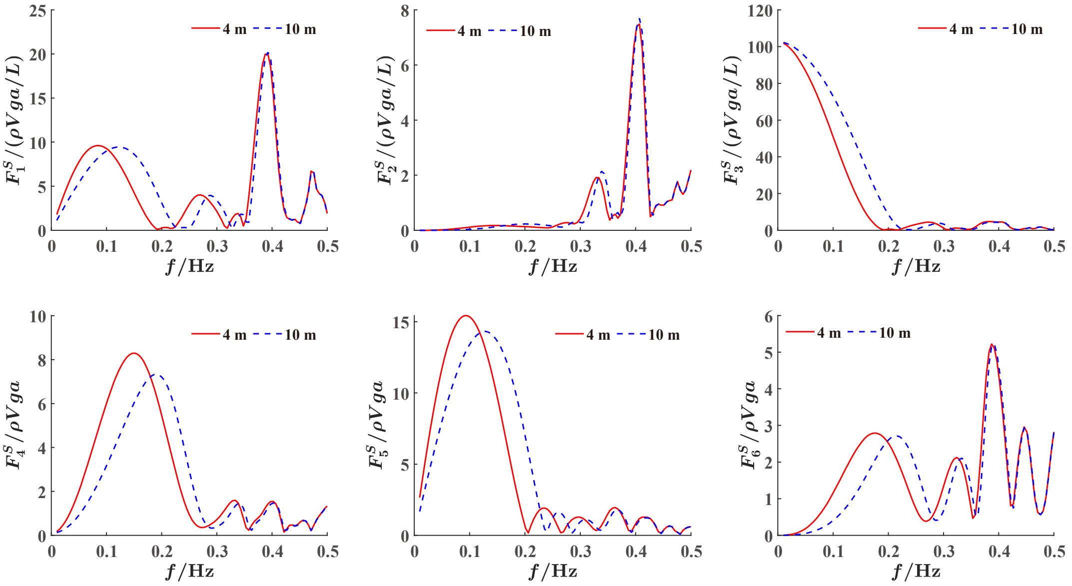

Fig. 11. Wave excitation force RAOs by WADAM.

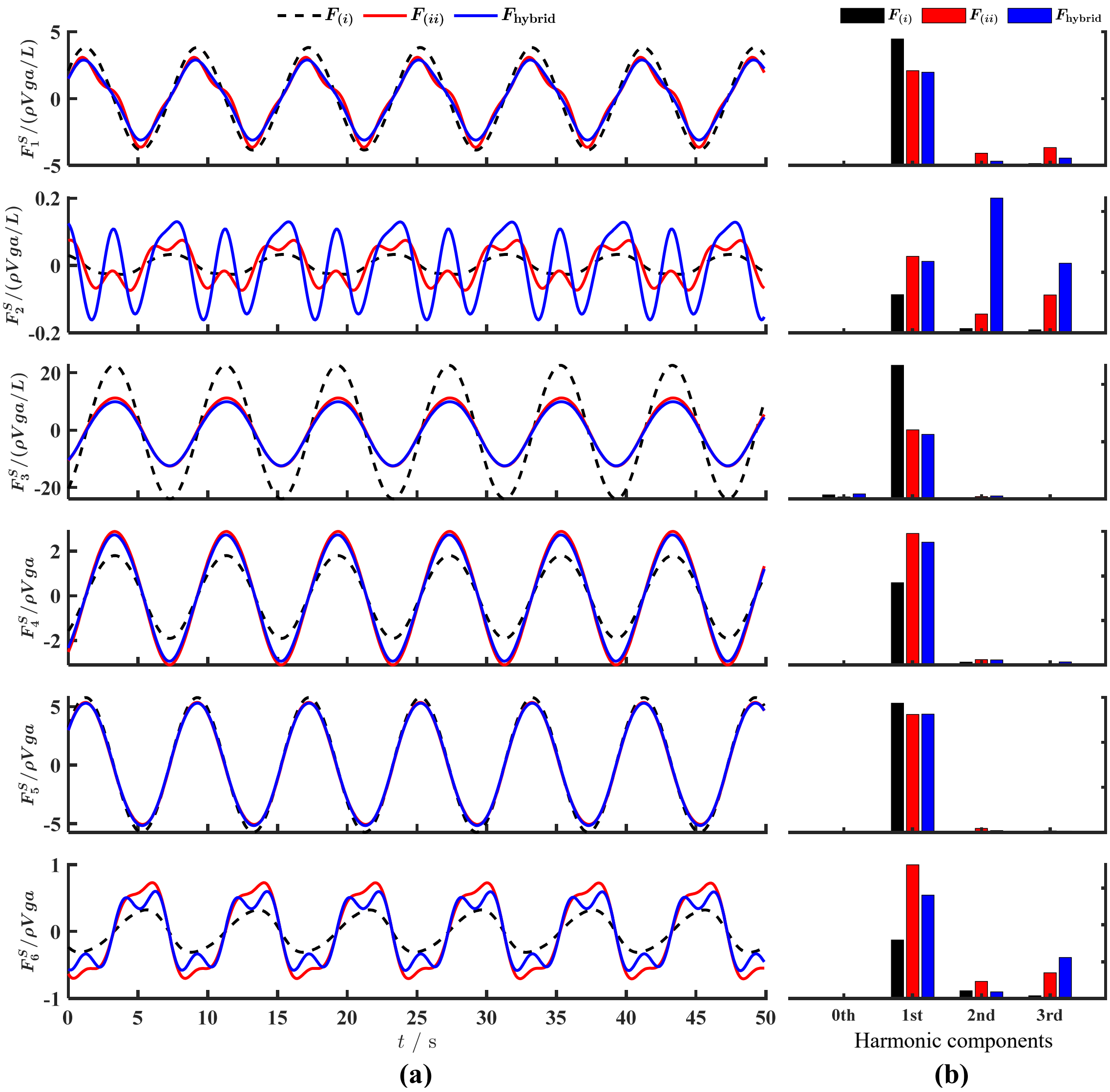

Fig. 12. 6-DoF wave forces comparison of V2: (a) Time domain; (b) Frequency domain.

The effectiveness of the HBPM in addressing oblique regular incident wave propagation over a slope is validated in V3, where the wave propagation direction is set at 30° relative to the positive *x*-axis. To eliminate lateral boundary reflection effects, FUNWAVE-TVD incorporates the periodicity strategy developed by Chen [56]. For effective implementation, this approach requires suitably extending the alongshore length to adhere to the periodicity assumption [57]. As illustrated in Fig. 13, implementing the periodic boundary condition successfully prevents the reflection of oblique waves, even without sponge layers at the lateral boundary. The snapshot demonstrates that, upon traversing the slope, the regular wave train undergoes nonlinear amplification and a deviation in its propagation direction, with the incident angle changing from 30.35° to 20.84°.

The comparison (Fig. 14) indicates that the wave excitation forces obtained by the HBPM closely align with those from LPM (ii). Consistent with the findings in V2, nonlinear deformation causes LPM (i) to overestimate the heave excitation forces. One of the arrangement axial lines of the triangular MFPV pontoons is oriented perpendicularly to the crest line of the 30° incident waves, rendering these oblique waves unable to produce yaw moments on the structure when using LPM (i). As noted earlier, oblique waves undergo a change in propagation direction after traversing the slope. Therefore, in LPM (ii), the wave excitation force RAO corresponds to waves with an incident direction of 20.84°. Additionally, the HBPM successfully captures the yaw moments induced by this phenomenon, where the magnitudes are modest but exhibit significant nonlinearity.

The configuration of V4 is designed to evaluate the computational performance of the HBPM under irregular wave conditions. The JONSWAP spectrum is discretized into 500 frequency bands, with a peak frequency of 0.125 Hz. Initially, a flat-bottomed scenario is established to validate the irregular wave generation capabilities of FUNWAVE-TVD. As depicted in Fig. 15, the simulation results closely align with the target spectrum. Additionally, Fig. 15 presents the wave spectrum at G2. The comparison between G1 spectrum and G2 spectrum reveals that seabed topography exerts a significant influence on irregular wave trains, leading to a noticeable reduction in energy, especially around the peak frequency. This underscores the importance of employing HBPM for hydrodynamic calculations of MFPV systems in such shallow-water environments. For the FUNWAVE-TVD simulations in V4, a total duration of 1500 s is utilized, with the latter 1000 s allocated for FFT analysis. For brevity, Fig. 16 presents only the time-domain results for 400 s. In the heave, pitch, sway, and roll directions, a perfect alignment between the HBPM and LPM (ii) is observed, while LPM (i) significantly overestimates the wave-induced forces in these directions, particularly near the peak frequency. This discrepancy arises from the substantial energy content at the peak frequency, which undergoes energy transfer upon encountering sloping terrain - a phenomenon that LPM (i) fails to capture. In the yaw direction, although there are discrepancies compared to the results from LPM (ii), the HBPM identifies multi-peak characteristics, while the wave-induced forces in the sway direction are overestimated.

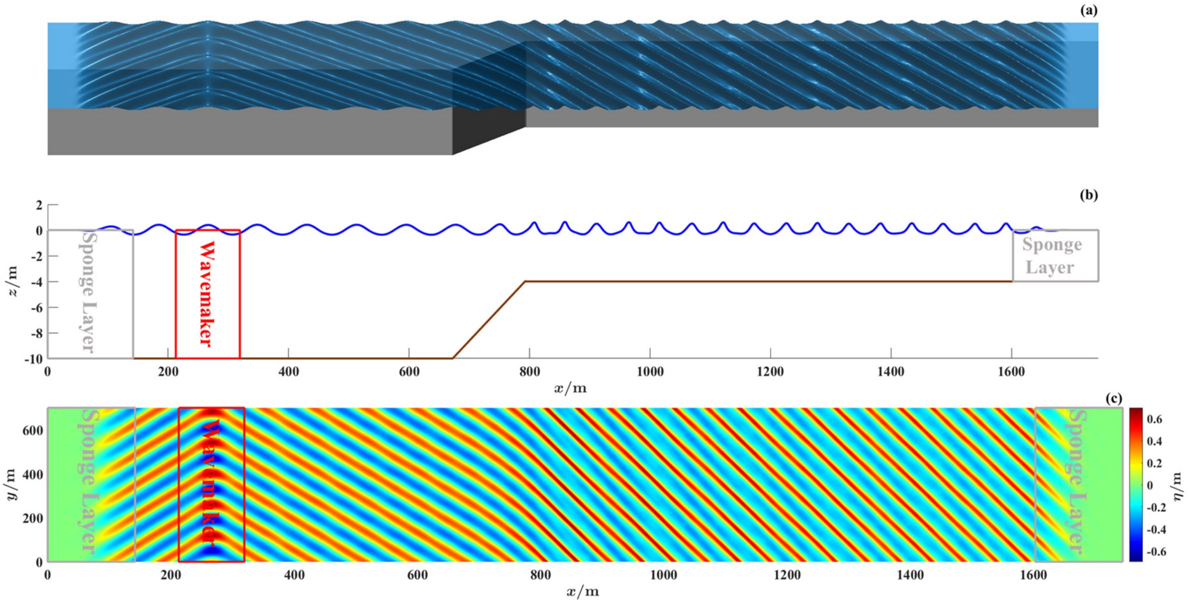

Fig. 13. Snapshot of V3 wave field at *t* = 250 s: (a) 3D view, (b) Side view, (c) Top view

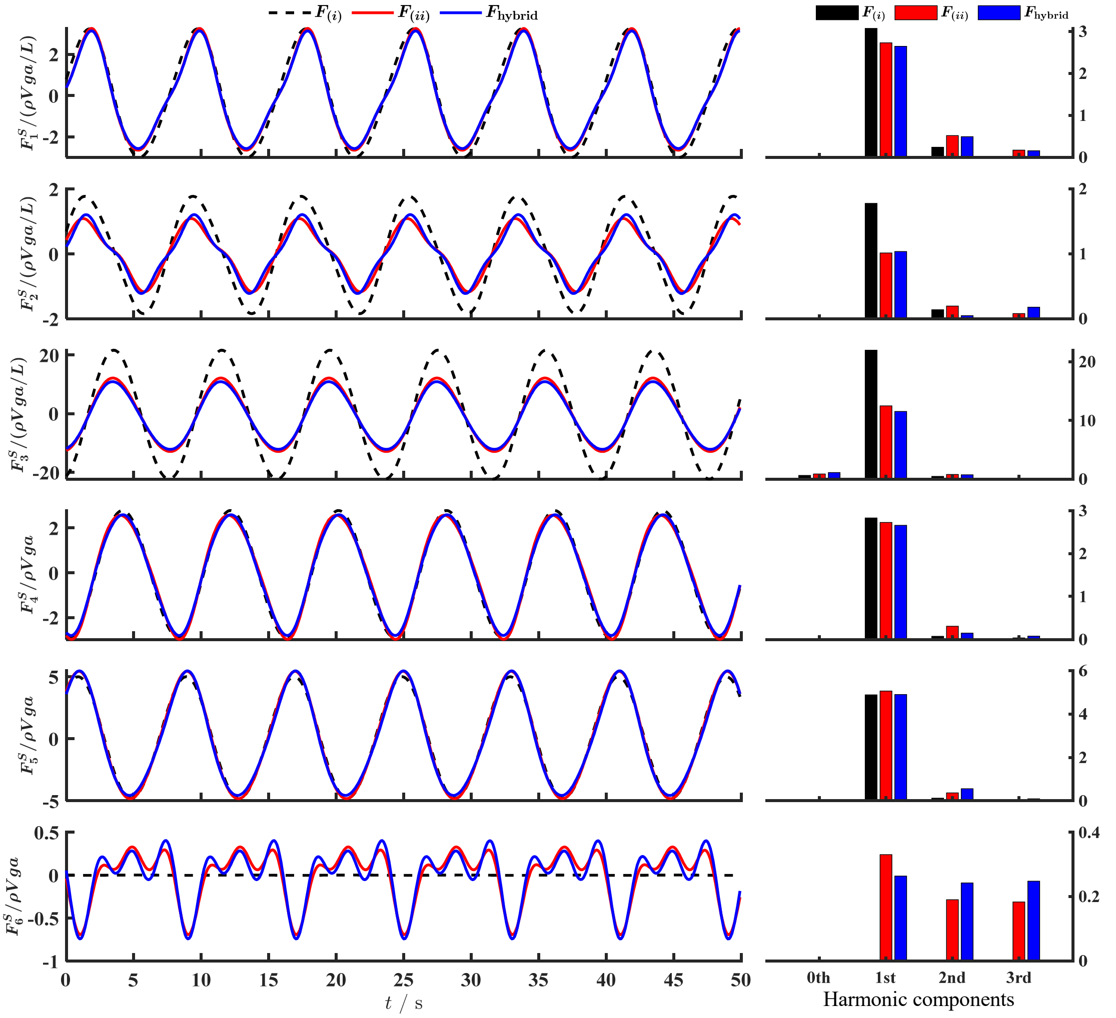

**(a)** **(b)**

Fig. 14. 6-DoF wave forces comparison of V3: (a) time domain, (b) frequency domain.

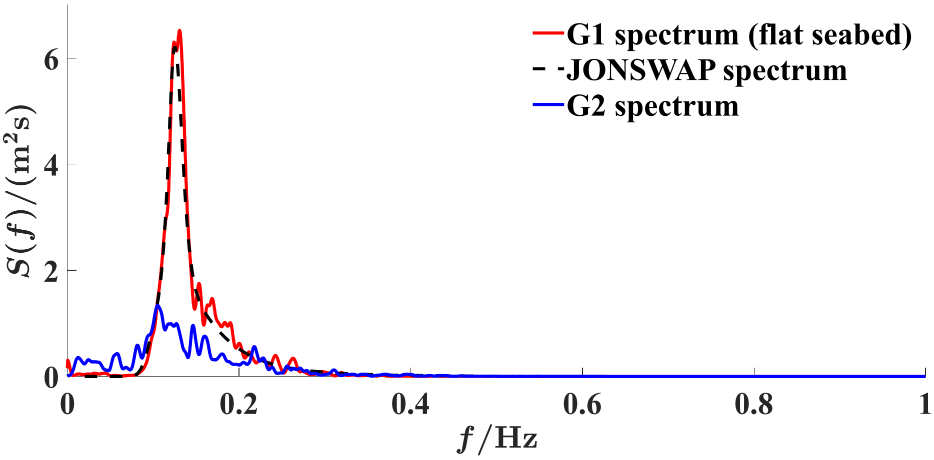

Fig. 15. Irregular wave generation validation of V4.

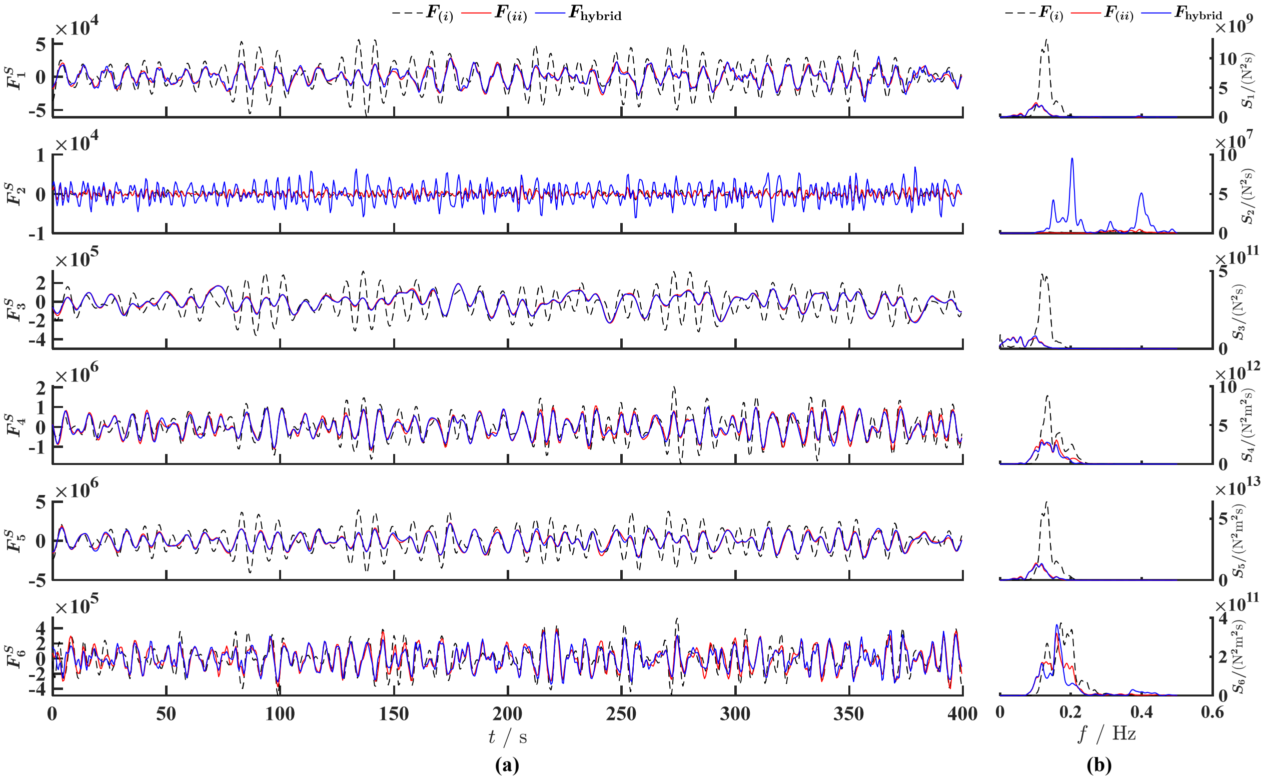

Fig. 16. 6-DoF wave forces comparison of V4: (a) time domain, (b) frequency domain.

### *3.1.3. Flat Topography with Partial Reflection*

The four examples discussed previously evaluated the accuracy of the HBPM without considering wave reflection from the right-side boundary. However, reflection from coastlines and littoral structures represents another critical factor affecting wave characteristics, which justifies the inclusion of V5. In FUNWAVE-TVD, a bottom-friction-type sponge layer is used, which has been demonstrated to be effective for modeling partially reflecting coastlines and breakwaters [58,59]. As depicted in Fig. 6c, the partially reflecting breakwater is modeled using an equivalent bottom-friction sponge layer, positioned $3L_{\mathrm{peak}}$ from the right-side sponge layer. The reflection coefficient is calculated using the Goda two-point method to match the predetermined value (0.4 in this study) and to determine the width and wave absorption coefficient of the breakwater. Following pre-testing, the breakwater's width and absorption coefficient are set at 30 m and 15.0, resulting in a reflection coefficient of 0.409, which closely approximates the target value. The wave generation parameters are consistent with those used in V4.

The distance $d_{12}$ between the two Goda wave gauges is set to 0.45 times the minimum wavelength $L_{\mathrm{min}}$ to avoid singularities in spectrum identification. The incident and reflected wave spectra, obtained using the Goda two-point method, are overlaid on the outcomes of WADAM computations for incidence angles of 0° and 180°, yielding $F_{\mathrm{Goda}}$. Fig. 17 illustrates that the HBPM exhibits commendable accuracy in calculating principal loads in environments with partial reflections.

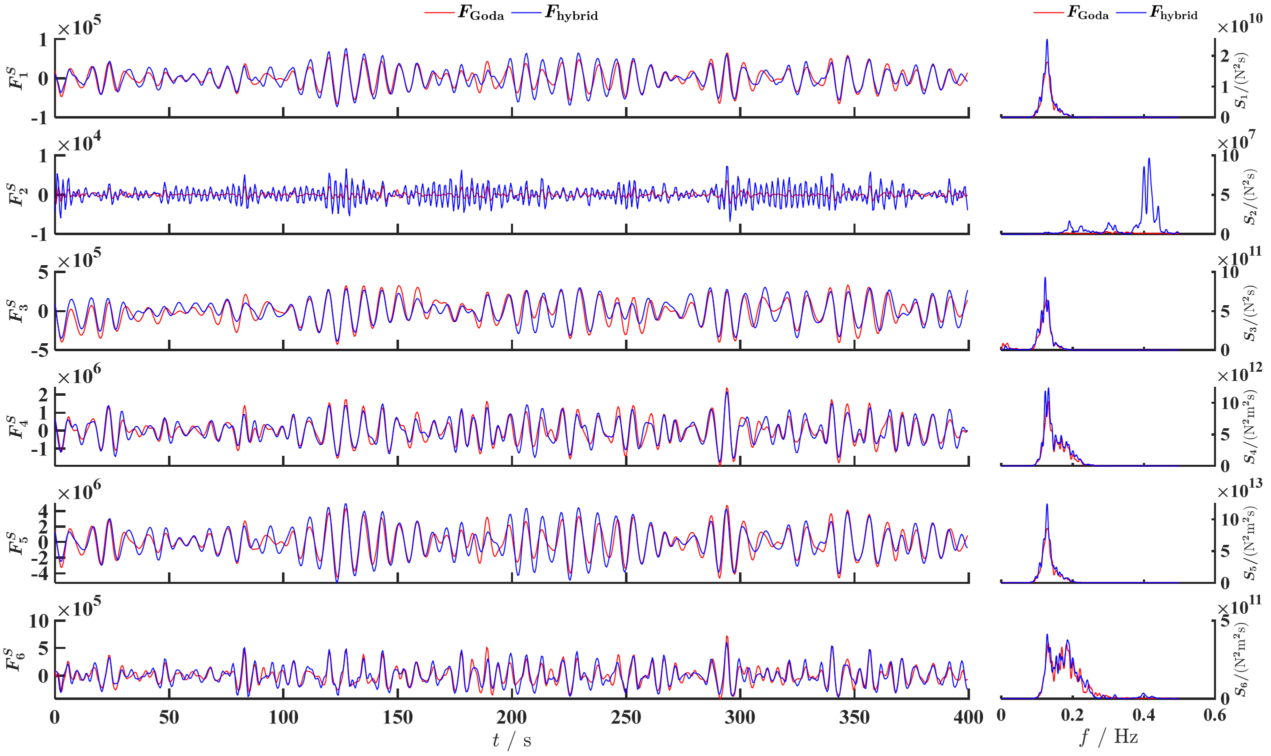

(a) (b)

Fig. 17. 6-DoF wave forces comparison of V5: (a) time domain, (b) frequency domain.

### 3.2. Radiation potential

Resolving the radiation problem is crucial for accurately determining the motion responses of floating photovoltaic systems. Given the linear nature of the three-dimensional potential problem in the inner region, radiation and scattering potentials can be addressed using two separate grid configurations (as shown in Fig. 5). Fig. 18 and Fig. 19 compare the hydrodynamic coefficients for MFPVs at a water depth of 4 meters, obtained using the panel method and WADAM. In this comparison, $S_c^R$ has a radius of 60 m, while $S_b^R$, $S_f^R$, and $S_c^R$ contain 5160, 8022, and 2355 elements, respectively. The analysis results confirm the accuracy of the panel model in addressing radiation potential.

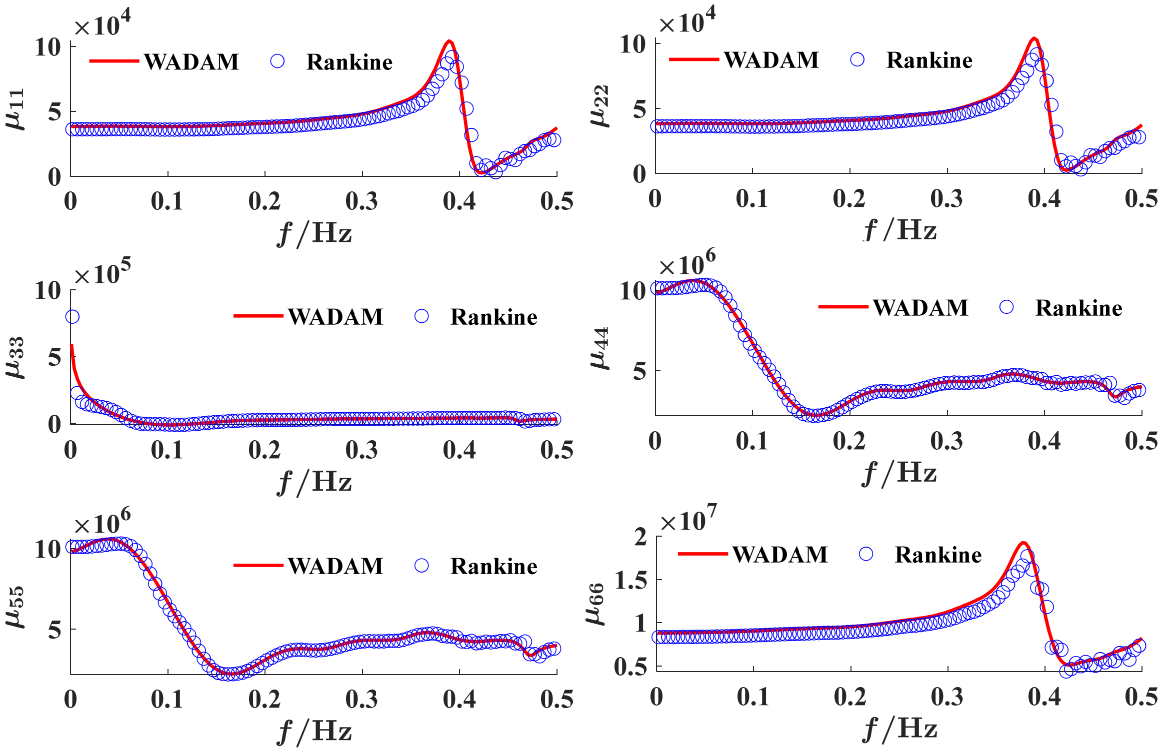

Fig. 18. MFPV added mass verification.

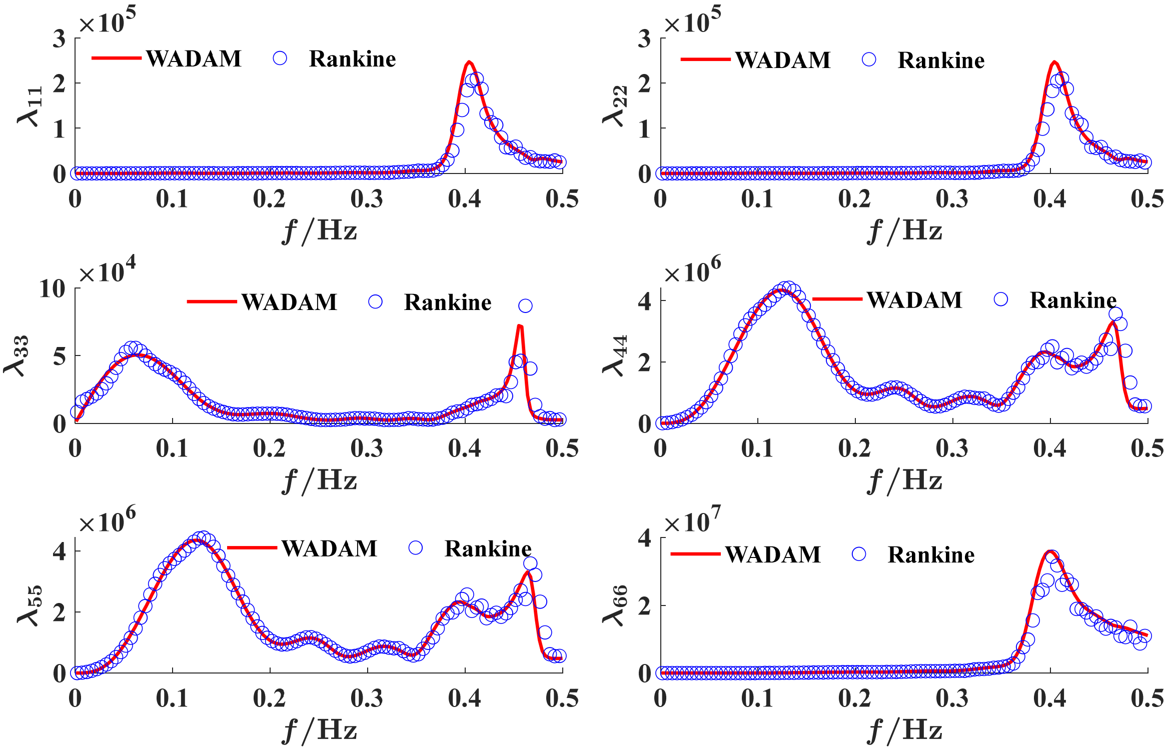

Fig. 19. MFPV potential damping verification.

## 4. Numerical case study

This chapter presents a hydrodynamic analysis of MFPV structures within typical nearshore environments utilizing the HBPM. The topography for the numerical case (Fig. 20a) is simplified based on the projected installation site (Fig. 2b), incorporating a uniform slope with a 1:20 gradient that connects the offshore area to the land. The wavemaker generates irregular unidirectional waves entering the bay, based on the JONSWAP spectrum with a peak period $T_p$ = 12 s and a significant wave height $H_{\text{sig}}$ = 2.0 m. In accordance with the sponge technique outlined in Section 3.1.3, a 20-meters-long, 600-meters-wide breakwater is positioned at the bay entrance to protect the MFPV. The remaining parameters of the breakwater and wavemaker remain consistent with those specified in V5. A sponge layer and lateral periodic boundary conditions are employed to mitigate unrealistic boundary reflections. MFPV installation locations $L_1$ through $L_6$ are established to examine the effects of irregular multidirectional wave fields on hydrodynamic coefficients, with each location featuring a control surface $S_c^S$ with a radius of 50 m. The total simulation duration is 2000 s, with the final 1500 s allocated for time-frequency transformation within the HBPM. Note that the local coordinate system orientation of the MFPV is consistent with the coordinate system definition in Fig. 20.

Fig. 20b presents a snapshot of the free surface elevation at $t$ = 1000 s in the numerical simulation. The breakwater exhibits significant wave dissipation capabilities, effectively reducing incident waves, which aligns with our engineering objectives. Fig. 21 compares the wave spectra at different installation positions, showing the highest wave energy at $L_4$.

This observation is anticipated, as $L_4$ is unprotected by the breakwater. The wave energy at $L_3$ is notably higher than at other protected locations due to its proximity to the breakwater entrance, which serves as the main entry point for wave energy. Fig. 20b also demonstrates that although the simulation utilizes unidirectional wave trains, the wave field exhibits complex multidirectional and non-uniform characteristics due to the influence of the coastlines and variable water depths. In this context, it is inappropriate to use fixed-point wave data at $L_1$ - $L_6$ directly for hydrodynamic calculations. Instead, the HBPM should be employed to account for the effects of the complex wave field on the MFPV.

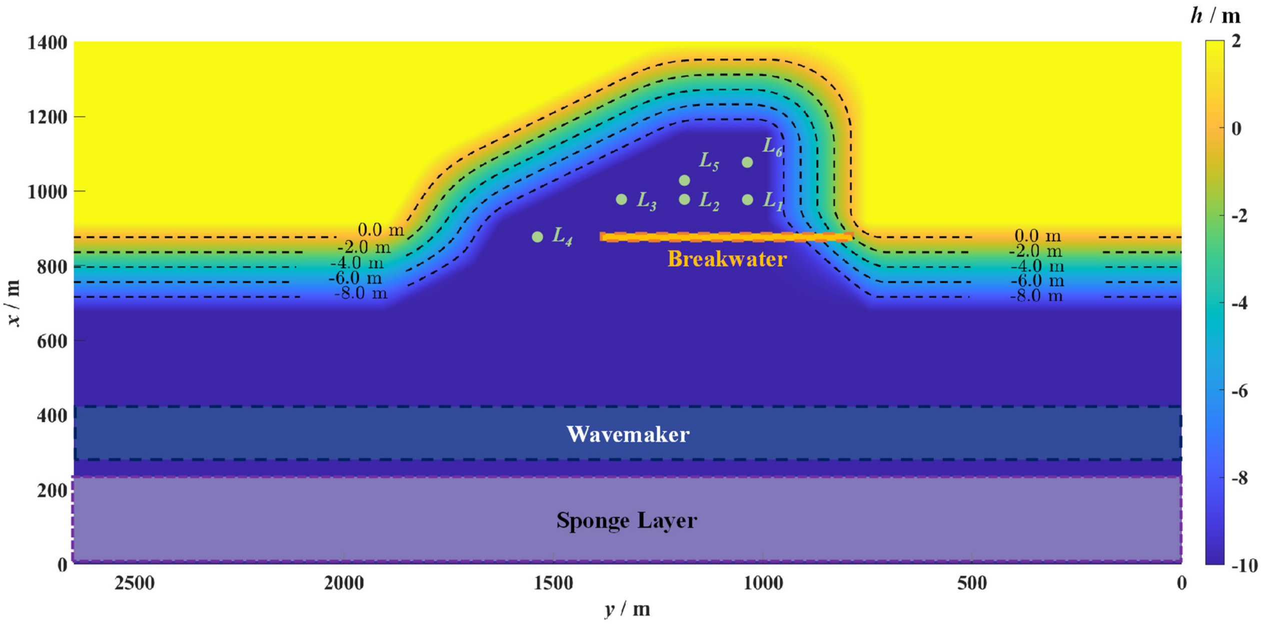

(a)

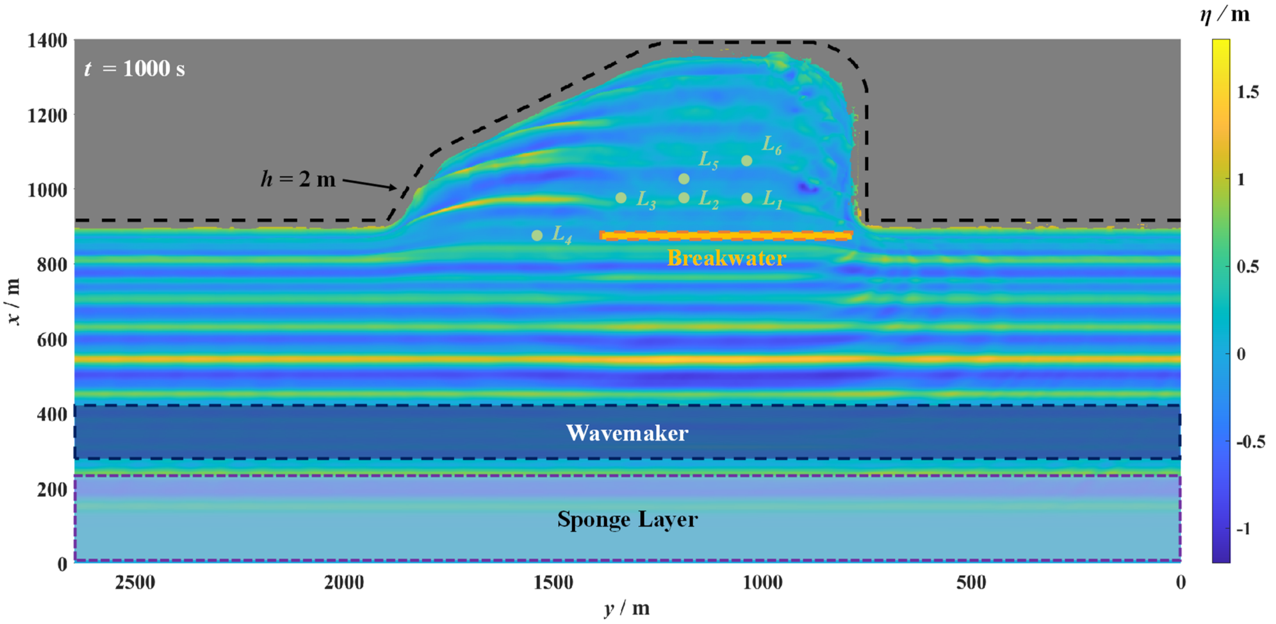

**(b)**

Fig. 20. (a) Numerical case topography, (b) Snapshot of wave simulation.

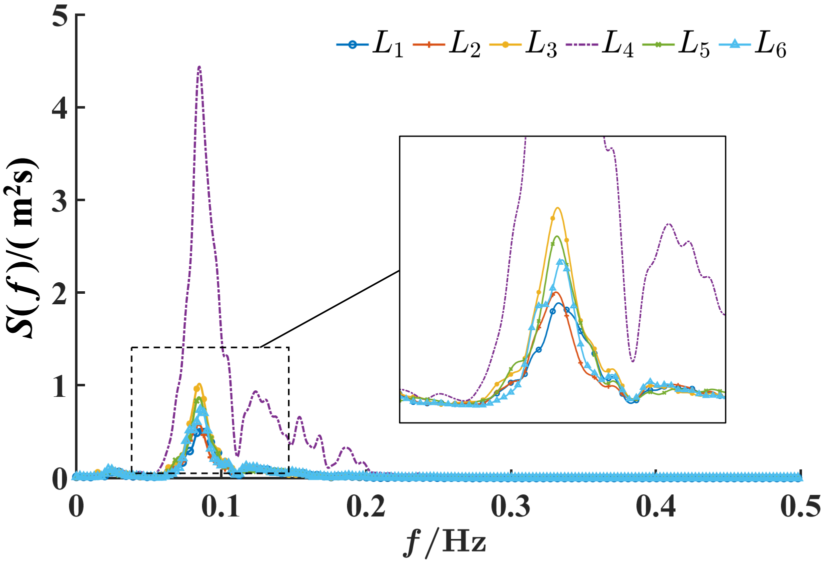

Fig. 21. Comparison of wave spectrum at installation location.

### 4.1. Wave excitation forces

Fig. 22 presents the spectral results of wave excitation forces obtained using the HBPM in the numerical case. It is evident that, with the exception of the sway direction, the breakwater substantially mitigates the wave forces exerted on the MFPV. At $L_4$, despite the presence of the highest wave energy, the sway force remains comparatively minimal. Likewise, the roll force exhibits no substantial difference in magnitude compared to breakwater-sheltered locations, this is a phenomenon that differs markedly from the behavior observed in the other four directions. The occurrence of above phenomenon can be attributed to the fact that the crest lines at $L_4$ remain relatively straight, without significant bending (Fig. 20b).

The sway and roll forces at $L_3$ and $L_5$ are markedly higher compared to other sheltered locations (Fig. 22), primarily due to their proximity to the breakwater entrance and the coastline, where waves display greater multidirectionality. The elevated sway forces at $L_3$ and $L_5$ would likely go undetected if calculations were conducted using the LPM, as the fixed-point wave spectrum results suggest minimal differences in wave energy between these locations and other sheltered areas.

Wave excitation forces in the *xoz* plane (surge, heave, and pitch) follow a similar pattern, with the most pronounced component occurring at the peak spectral frequency ($f_{\mathrm{peak}}$ = 0.0833 Hz). Unlike the sheltered regions, these three force components at $L_4$ exhibit not only higher energy but also substantial higher-order components, with frequencies primarily around 0.123 Hz, possibly related to the bay's resonant frequency.

In summary, the HBPM results demonstrate that the wave excitation forces on the MFPV are profoundly affected by the multidirectional and non-uniform nature of the wave field, resulting from topographic variations and shoreline reflections. This underscores the greater suitability of HBPM over LPM in nearshore bay environments.

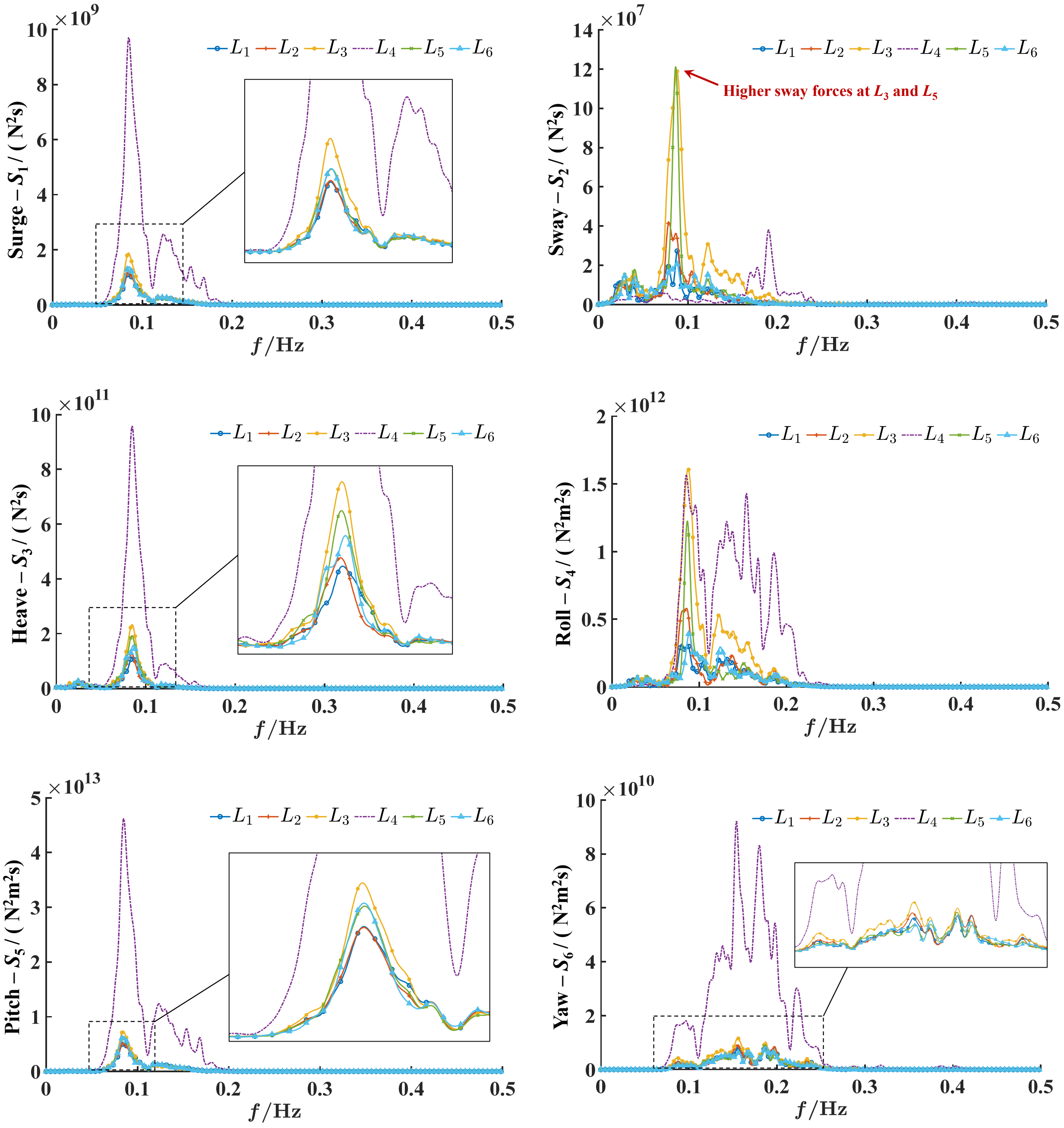

Fig. 22. 6-DoF MPFV wave excitation forces obtained by HBPM.

### *4.2. Wave-induced motions*

It can be anticipated that non-uniform, multi-directional irregular waves will lead to more complex motion responses in MFPV. According to the computational procedure outlined in the HBPM, once the wave excitation forces are computed, the wave-induced motions of the MFPV can be efficiently solved using linear motion equations, incorporating the radiation hydrodynamic coefficients described in Section 3.2. Fig. 23 illustrates the 6-DoF motion results derived from the HBPM. Similar to the results for wave excitation forces, the motion at $L_4$ predominates across all positions except in the sway direction. This indicates the potential of the breakwater to effectively constrain the motion within acceptable limits.

At sheltered locations, the sway motion exhibits a notable low-frequency characteristic, with energy levels that significantly surpass the peak frequency component. In contrast, motions in other directions are predominantly concentrated around the input peak frequency. Therefore, despite the significant changes in wave characteristics and propagation direction caused by the coastline, varying water depths, and breakwater, the motion at the input peak frequency remains a crucial factor to consider.

According to the computational results, $L_1$ displays the smallest motion amplitude, excluding the yaw direction, whereas $L_3$ experiences the most significant motion within the sheltered zones. Comparisons between $L_2$ and $L_5$, as well as between $L_1$ and $L_6$, reveal that motion is more pronounced farther from the breakwater. Consequently, $L_1$ emerges as the optimal location for installing the single MFPV module. In practical engineering scenarios, it is advisable to position the installation site as far from the breakwater entrance as possible while remaining in close proximity to the breakwater. It is important to note that these conclusions are derived solely from the numerical case established in this study.

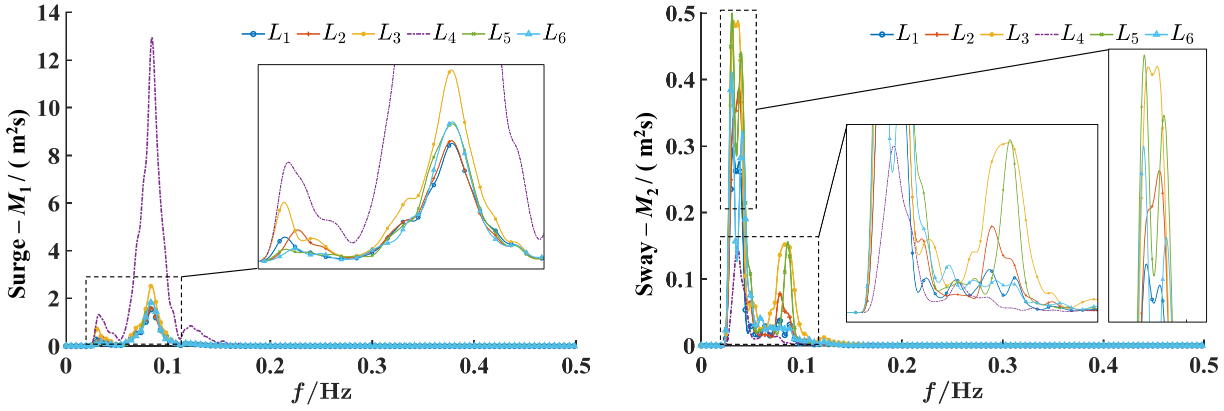

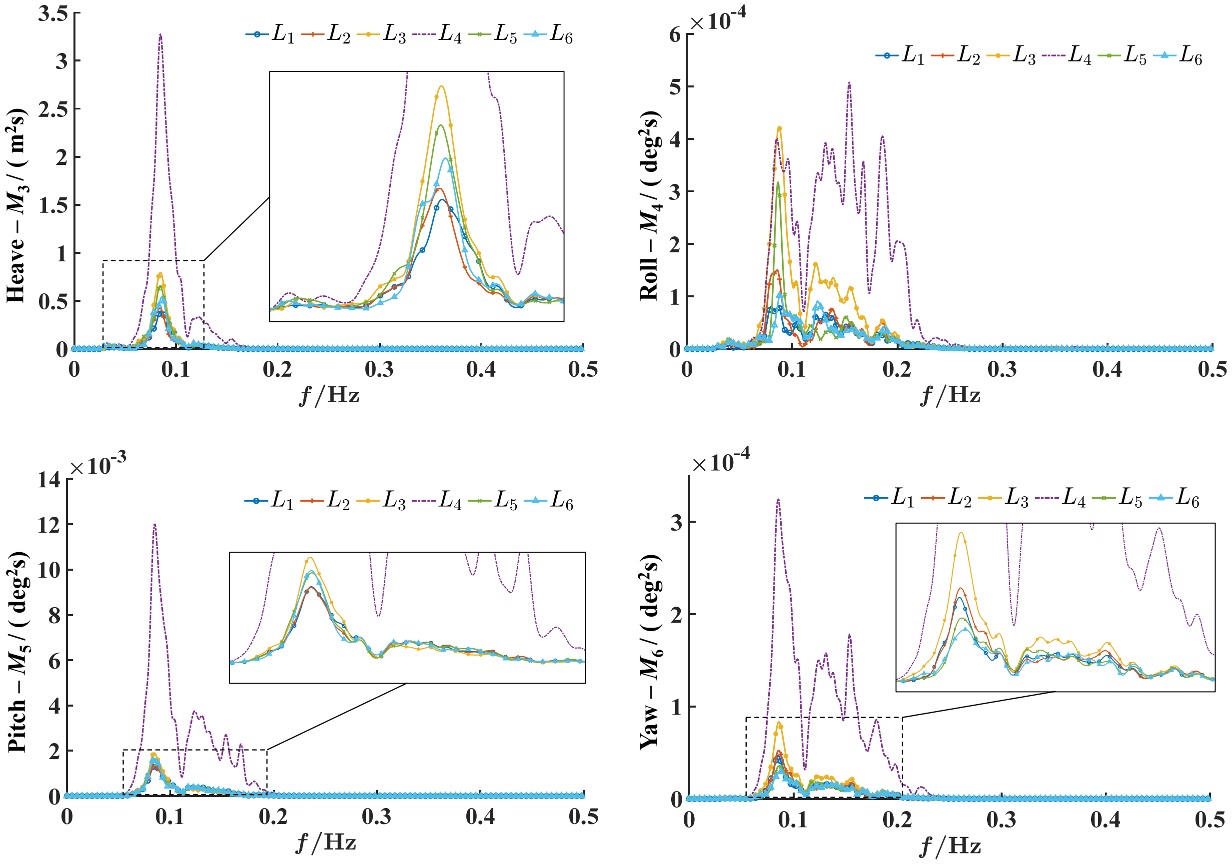

Fig. 23. 6-DoF MPFV motions obtained by HBPM.

## 5. Conclusions

This paper applies a hybrid Boussinesq-Panel method (HBPM) for the hydrodynamic analysis of a novel marine floating photovoltaics (MFPV) structure in nearshore shallow water environments. The HBPM is validated through a series of test cases involving triangular frame MFPV structures and subsequently applied to a numerically case that approximates real projected installation conditions. The conclusions drawn are as follows:

(1) The first three cases validate the computational effectiveness of the HBPM under regular wave conditions, confirming its accuracy in predicting dominant wave loads. Furthermore, the cases involving sloped terrains demonstrate that waves experience substantial nonlinear deformation and directional shifts upon interacting with slopes, leading to inaccuracies in traditional methods reliant on offshore data.

(2) The HBPM performs effectively under irregular wave conditions. Analysis of sloped terrains and numerical breakwater scenarios highlights its capability to capture nonlinear wave deformations in shallow water and accurately model wave reflections. Notably, in the numerical breakwater case, there is a remarkable agreement between the results obtained from the HBPM and those derived from the incident-reflection separation technique.

(3) In typical shallow water numerical case, the environment's complexity causes unidirectional wave trains to exhibit significant multidirectional non-uniformity upon entering the bay. Both wave simulations and results from the HBPM

confirm the shielding effect of the numerical breakwater. Generally, the wave excitation forces on the MFPV are markedly reduced in sheltered regions compared to those near the entrance. However, attention should be paid to areas adjacent to the entrance and distant from the breakwater (e.g., $L_3$ and $L_5$), as the sway force can increase in these locations. According to the HBPM results, to minimize motion response, it is advisable to position the MFPV in regions distant from the entrance and near the breakwater, such as at location $L_1$.

Drawing from the insights and findings presented in this paper, the nonlinear evolution of waves, combined with changes in propagation direction due to variations in shallow water depth and coastline reflections, will substantially impact on the hydrodynamic performance of the MFPV. Furthermore, numerous avenues for future enhancement of the HBPM exist, including but not limited to: incorporating real-sea terrain, accounting for variable water depths in the inner region, and conducting multi-body array calculations. Additionally, the proposed method in this study has certain limitations, such as the current exclusion of the influence of inner domain waves on the outer domain and the omission of hydroelastic effects of MFPV. These aspects represent important directions for future research and development.

## Acknowledgements

This study is supported by the National Natural Science Foundation of China (No. 52088102 and 52101339) and the Key R&D projects of Shandong Province (No. 2021ZLGX04).

## References

[1] IEA, “World Energy Outlook 2023,” IEA, Paris, 2023. Accessed: Jul. 10, 2024. [Online]. Available: https://www.iea.org/reports/world-energy-outlook-2023

[2] W. Shi *et al.*, “Review on the development of marine floating photovoltaic systems,” *Ocean Engineering*, vol. 286, p. 115560, Oct. 2023, doi: 10.1016/j.oceaneng.2023.115560.

[3] Z. Jiang *et al.*, “Design and model test of a soft-connected lattice-structured floating solar photovoltaic concept for harsh offshore conditions,” *Marine Structures*, vol. 90, p. 103426, Jul. 2023, doi: 10.1016/j.marstruc.2023.103426.

[4] B. Bai, S. Xiong, X. Ma, and X. Liao, “Assessment of floating solar photovoltaic potential in China,” *Renewable Energy*, p. 119572, Nov. 2023, doi: 10.1016/j.renene.2023.119572.

[5] M. Deveci, D. Pamucar, and E. Oguz, “Floating photovoltaic site selection using fuzzy rough numbers based LAAW and RAFSI model,” *Applied Energy*, vol. 324, p. 119597, Oct. 2022, doi: 10.1016/j.apenergy.2022.119597.

[6] G. Kakoulaki *et al.*, “Benefits of pairing floating solar photovoltaics with hydropower reservoirs in Europe,” *Renewable and Sustainable Energy Reviews*, vol. 171, p. 112989, Jan. 2023, doi: 10.1016/j.rser.2022.112989.

[7] H. Pouran, M. Padilha Campos Lopes, H. Ziar, D. Alves Castelo Branco, and Y. Sheng, “Evaluating floating photovoltaics (FPVs) potential in providing clean energy and supporting agricultural growth in Vietnam,” *Renewable and Sustainable Energy Reviews*, vol. 169, p. 112925, Nov. 2022, doi: 10.1016/j.rser.2022.112925.

[8] C. Zhang, J. Dai, K. K. Ang, and H. V. Lim, “Development of compliant modular floating photovoltaic farm for coastal conditions,” *Renewable and Sustainable Energy Reviews*, vol. 190, p. 114084, Feb. 2024, doi:

10.1016/j.rser.2023.114084.

[9] R. Gonzalez Sanchez, I. Kougias, M. Moner-Girona, F. Fahl, and A. Jäger-Waldau, "Assessment of floating solar photovoltaics potential in existing hydropower reservoirs in Africa," *Renewable Energy*, vol. 169, pp. 687–699, May 2021, doi: 10.1016/j.renene.2021.01.041.

[10] L. Micheli and D. L. Talavera, "Economic feasibility of floating photovoltaic power plants: Profitability and competitiveness," *Renewable Energy*, vol. 211, pp. 607–616, Jul. 2023, doi: 10.1016/j.renene.2023.05.011.

[11] J. Nasir, A. Javed, M. Ali, K. Ullah, and S. A. A. Kazmi, "Sustainable and cost-effective hybrid energy solution for arid regions: Floating solar photovoltaic with integrated pumped storage and conventional hydropower," *Journal of Energy Storage*, vol. 74, p. 109417, Dec. 2023, doi: 10.1016/j.est.2023.109417.

[12] P. Ranjbaran, H. Yousefi, G. B. Gharehpetian, and F. R. Astaraei, "A review on floating photovoltaic (FPV) power generation units," *Renewable and Sustainable Energy Reviews*, vol. 110, pp. 332–347, Aug. 2019, doi: 10.1016/j.rser.2019.05.015.

[13] T. Bajc and D. Kostadinović, "Potential of usage of the floating photovoltaic systems on natural and artificial lakes in the Republic of Serbia," *Journal of Cleaner Production*, vol. 422, p. 138598, Oct. 2023, doi: 10.1016/j.jclepro.2023.138598.

[14] A. Boduch, K. Mik, R. Castro, and P. Zawadzki, "Technical and economic assessment of a 1 MWp floating photovoltaic system in Polish conditions," *Renewable Energy*, vol. 196, pp. 983–994, Aug. 2022, doi: 10.1016/j.renene.2022.07.032.

[15] S. Gorjian, H. Sharon, H. Ebadi, K. Kant, F. B. Scavo, and G. M. Tina, "Recent technical advancements, economics and environmental impacts of floating photovoltaic solar energy conversion systems," *Journal of Cleaner Production*, vol. 278, p. 124285, Jan. 2021, doi: 10.1016/j.jclepro.2020.124285.

[16] M. I. Kulat, K. Tosun, A. B. Karaveli, I. Yucel, and B. G. Akinoglu, "A sound potential against energy dependency and climate change challenges: Floating photovoltaics on water reservoirs of Turkey," *Renewable Energy*, vol. 206, pp. 694–709, Apr. 2023, doi: 10.1016/j.renene.2022.12.058.

[17] E. Muñoz-Cerón, J. C. Osorio-Aravena, F. J. Rodríguez-Segura, M. Frolova, and A. Ruano-Quesada, "Floating photovoltaics systems on water irrigation ponds: Technical potential and multi-benefits analysis," *Energy*, vol. 271, p. 127039, May 2023, doi: 10.1016/j.energy.2023.127039.

[18] Z. Jin, Y. Liu, M. Zhu, H. Fang, and A. Li, "A novel analytical model coupling hydrodynamic-structural-material scales for very large floating photovoltaic support structures," *Ocean Engineering*, vol. 275, p. 114113, May 2023, doi: 10.1016/j.oceaneng.2023.114113.

[19] Y. Shi, Y. Wei, Z. Y. Tay, and Z. Chen, "Hydroelastic analysis of offshore floating photovoltaic based on frequency-domain model," *Ocean Engineering*, vol. 289, p. 116213, Dec. 2023, doi: 10.1016/j.oceaneng.2023.116213.

[20] Z. Li, D. Chen, and X. Feng, "Hydroelastic and expansibility analysis of a modular floating photovoltaic system with multi-directional hinge connections," *Ocean Engineering*, vol. 289, p. 116218, Dec. 2023, doi: 10.1016/j.oceaneng.2023.116218.

[21] J. Song, J. Kim, W. C. Chung, D. Jung, Y. J. Kang, and S. Kim, "Wave-induced structural response analysis of the supporting frames for multiconnected offshore floating photovoltaic units installed in the inner harbor," *Ocean Engineering*, vol. 271, p. 113812, Mar. 2023, doi: 10.1016/j.oceaneng.2023.113812.

[22] R. Claus and M. López, "A methodology to assess the dynamic response and the structural performance of floating photovoltaic systems," *Solar Energy*, vol. 262, p. 111826, Sep. 2023, doi: 10.1016/j.solener.2023.111826.

[23] S. M. Choi, C.-D. Park, S.-H. Cho, and B.-J. Lim, "Effects of various inlet angle of wind and wave loads on

floating photovoltaic system considering stress distributions," *Journal of Cleaner Production*, vol. 387, p. 135876, Feb. 2023, doi: 10.1016/j.jclepro.2023.135876.

[24] A. M. Bassam *et al.*, "Conceptual design of a novel partially floating photovoltaic integrated with smart energy storage and management system for Egyptian North Lakes," *Ocean Engineering*, vol. 279, p. 114416, Jul. 2023, doi: 10.1016/j.oceaneng.2023.114416.

[25] J. Du, D. Zhang, Y. Zhang, K. Xu, A. Chang, and S. Zhao, "Design and comparative analysis of alternative mooring systems for offshore floating photovoltaics arrays in ultra-shallow water with significant tidal range," *Ocean Engineering*, vol. 302, p. 117649, Jun. 2024, doi: 10.1016/j.oceaneng.2024.117649.

[26] D. Zhang, J. Du, Z. Yuan, S. Yu, and H. Li, "Motion characteristics of large arrays of modularized floating bodies with hinge connections," *Physics of Fluids*, vol. 35, no. 7, p. 077107, Jul. 2023, doi: 10.1063/5.0153317.

[27] "Floating Solar PV for the Sea - SolarSea. Rooftop solar for islands," Swimsol. Accessed: Sep. 05, 2024. [Online]. Available: https://swimsol.com/

[28] "Sunseap installs one of world's largest offshore floating solar farms in Singapore," Offshore Energy. Accessed: Sep. 05, 2024. [Online]. Available: https://www.offshore-energy.biz/sunseap-installs-one-of-worlds-largest-offshore-floating-solar-farms-in-singapore/

[29] B. Buchner, "The Motions of a Ship on a Sloped Seabed," in *Volume 1: Offshore Technology; Offshore Wind Energy; Ocean Research Technology; LNG Specialty Symposium*, Hamburg, Germany: ASMEDC, Jan. 2006, pp. 339–347. doi: 10.1115/OMAE2006-92321.

[30] P. Teigen, "Motion response of a spread moored barge over a sloping bottom," presented at the ISOPE International Ocean and Polar Engineering Conference, Seoul, Korea, Jun. 2005.

[31] A. Feng, H. Cai, and Y. You, "Freely floating body motion responses induced by wave and current in seabed conditions," *Ocean Engineering*, vol. 172, pp. 396–406, Jan. 2019, doi: 10.1016/j.oceaneng.2018.12.002.

[32] T. Kim and Y. Kim, "Numerical analysis on floating-body motion responses in arbitrary bathymetry," *Ocean Engineering*, vol. 62, pp. 123–139, Apr. 2013, doi: 10.1016/j.oceaneng.2013.01.012.

[33] A. P. Engsig-Karup, H. B. Bingham, and O. Lindberg, "An efficient flexible-order model for 3D nonlinear water waves," *Journal of Computational Physics*, vol. 228, no. 6, pp. 2100–2118, Apr. 2009, doi: 10.1016/j.jcp.2008.11.028.

[34] X. Feng and W. Bai, "Wave resonances in a narrow gap between two barges using fully nonlinear numerical simulation," *Applied Ocean Research*, vol. 50, pp. 119–129, Mar. 2015, doi: 10.1016/j.apor.2015.01.003.

[35] E. Guerber, M. Benoit, S. T. Grilli, and C. Buvat, "A fully nonlinear implicit model for wave interactions with submerged structures in forced or free motion," *Engineering Analysis with Boundary Elements*, vol. 36, no. 7, pp. 1151–1163, Jul. 2012, doi: 10.1016/j.enganabound.2012.02.005.

[36] S.-J. Choi, K.-H. Lee, and O. T. Gudmestad, "The effect of dynamic amplification due to a structure's vibration on breaking wave impact," *Ocean Engineering*, vol. 96, pp. 8–20, Mar. 2015, doi: 10.1016/j.oceaneng.2014.11.012.

[37] L.-C. Dempwolff, C. Windt, H. Bihs, G. Melling, I. Holzwarth, and N. Goseberg, "Hydrodynamic coupling of multi-fidelity solvers in REEF3D with application to ship-induced wave modelling," *Coastal Engineering*, vol. 188, p. 104452, Mar. 2024, doi: 10.1016/j.coastaleng.2023.104452.

[38] W. Mo, A. Jensen, and P. L.-F. Liu, "Plunging solitary wave and its interaction with a slender cylinder on a sloping beach," *Ocean Engineering*, vol. 74, pp. 48–60, Dec. 2013, doi: 10.1016/j.oceaneng.2013.09.011.

[39] H. Xiao and W. Huang, "Three-Dimensional Numerical Modeling of Solitary Wave Breaking and Force on a Cylinder Pile in a Coastal Surf Zone," *J. Eng. Mech.*, vol. 141, no. 8, p. A4014001, Aug. 2015, doi: 10.1061/(ASCE)EM.1943-7889.0000834.

[40] H. B. Bingham, “A hybrid Boussinesq-panel method for predicting the motion of a moored ship,” *Coastal Engineering*, vol. 40, no. 1, pp. 21–38, Apr. 2000, doi: 10.1016/S0378-3839(00)00002-8.

[41] Z. Zheng, X. Ma, M. Yan, Y. Ma, and G. Dong, “Hydrodynamic response of moored ships to seismic-induced harbor oscillations,” *Coastal Engineering*, vol. 176, p. 104147, Sep. 2022, doi: 10.1016/j.coastaleng.2022.104147.

[42] P. Yang, “Boussinesq-Hydroelasticity coupled model to investigate hydroelastic responses and connector loads of an eight-module VLFS near islands in time domain,” *Ocean Engineering*, 2019.

[43] J. Ding *et al.*, “Numerical and experimental investigation on hydroelastic responses of an 8-module VLFS near a typical island,” *Ocean Engineering*, vol. 214, p. 107841, Oct. 2020, doi: 10.1016/j.oceaneng.2020.107841.

[44] J. L. Hess and A. M. O. Smith, “Calculation of Nonlifting Potential Flow About Arbitrary Three-Dimensional Bodies,” *Journal of Ship Research*, vol. 8, no. 04, pp. 22–44, Sep. 1964, doi: 10.5957/jsr.1964.8.4.22.

[45] F. Shi, J. T. Kirby, J. C. Harris, J. D. Geiman, and S. T. Grilli, “A high-order adaptive time-stepping TVD solver for Boussinesq modeling of breaking waves and coastal inundation,” *Ocean Modelling*, vol. 43–44, pp. 36–51, Jan. 2012, doi: 10.1016/j.ocemod.2011.12.004.

[46] Y.-K. Choi, F. Shi, M. Malej, and J. M. Smith, “Performance of various shock-capturing-type reconstruction schemes in the Boussinesq wave model, FUNWAVE-TVD,” *Ocean Modelling*, vol. 131, pp. 86–100, Nov. 2018, doi: 10.1016/j.ocemod.2018.09.004.

[47] J. Gao, C. Ji, O. Gaidai, Y. Liu, and X. Ma, “Numerical investigation of transient harbor oscillations induced by N-waves,” *Coastal Engineering*, vol. 125, pp. 119–131, Jul. 2017, doi: 10.1016/j.coastaleng.2017.03.004.

[48] C. Liu, Y. Onat, Y. Jia, and J. O’Donnell, “Modeling nearshore dynamics of extreme storms in complex environments of Connecticut,” *Coastal Engineering*, vol. 168, p. 103950, Sep. 2021, doi: 10.1016/j.coastaleng.2021.103950.

[49] O. Nwogu, “Alternative Form of Boussinesq Equations for Nearshore Wave Propagation,” *J. Waterway, Port, Coastal, Ocean Eng.*, vol. 119, no. 6, pp. 618–638, Nov. 1993, doi: 10.1061/(ASCE)0733-950X(1993)119:6(618).

[50] A. B. Kennedy, J. T. Kirby, Q. Chen, and R. A. Dalrymple, “Boussinesq-type equations with improved nonlinear performance,” *Wave Motion*, vol. 33, no. 3, pp. 225–243, Mar. 2001, doi: 10.1016/S0165-2125(00)00071-8.

[51] Q. Chen, “Fully Nonlinear Boussinesq-Type Equations for Waves and Currents over Porous Beds,” *J. Eng. Mech.*, vol. 132, no. 2, pp. 220–230, Feb. 2006, doi: 10.1061/(ASCE)0733-9399(2006)132:2(220).

[52] M. Torres, M.-A. Lam, and M. Malej, “Practical guidance for numerical modeling in FUNWAVE-TVD,” Engineer Research and Development Center (U.S.), Oct. 2022. doi: 10.21079/11681/45641.

[53] S.-L. James Hu, W.-L. Yang, and H.-J. Li, “Signal decomposition and reconstruction using complex exponential models,” *Mechanical Systems and Signal Processing*, vol. 40, no. 2, pp. 421–438, Nov. 2013, doi: 10.1016/j.ymssp.2013.06.037.

[54] K. Zhao, Y. Wang, and P. L.-F. Liu, “A guide for selecting periodic water wave theories - Le Méhauté (1976)’s graph revisited,” *Coastal Engineering*, vol. 188, p. 104432, Mar. 2024, doi: 10.1016/j.coastaleng.2023.104432.

[55] J. D. Fenton and M. M. Rienecker, “A Fourier method for solving nonlinear water-wave problems: application to solitary-wave interactions,” *J. Fluid Mech.*, vol. 118, no. 1, p. 411, May 1982, doi: 10.1017/S0022112082001141.

[56] Q. Chen, J. T. Kirby, R. A. Dalrymple, F. Shi, and E. B. Thornton, “Boussinesq modeling of longshore currents,” *J. Geophys. Res.*, vol. 108, no. C11, p. 2002JC001308, Nov. 2003, doi: 10.1029/2002JC001308.

[57] M. Malej, F. Shi, J. M. Smith, G. Cuomo, and N. Tozer, “Boussinesq-Type Modeling of Low-Frequency Wave Motions at Marina di Carrara,” *J. Waterway, Port, Coastal, Ocean Eng.*, vol. 147, no. 6, p. 05021015, Nov. 2021, doi: 10.1061/(ASCE)WW.1943-5460.0000676.

[58] M. Yan, Z. Zheng, Z. Sun, X. Ma, and G. Dong, “Numerical evaluation of the tension mooring effects on the

hydrodynamic response of moored ships under harbor oscillations," *Ocean Engineering*, vol. 288, p. 116127, Nov. 2023, doi: 10.1016/j.oceaneng.2023.116127.

[59] Z. Zheng, X. Ma, Y. Ma, and G. Dong, "Wave estimation within a port using a fully nonlinear Boussinesq wave model and artificial neural networks," *Ocean Engineering*, vol. 216, p. 108073, Nov. 2020, doi: 10.1016/j.oceaneng.2020.108073.